Shear-induced mixing in geophysical flows: does the route to turbulence matter to its efficiency?

A. Mashayek† and W. R. Peltier

Department of Physics, University of Toronto, Ontario, Canada M5S 1A7

Motivated by the importance of diapycnal mixing parameterizations in large-scale ocean general circulation models, we provide a detailed analysis of high-Reynolds-number mixing in density stratified shear flows which constitute an archetypical example of the small-scale physical processes occurring in the oceanic interior that control turbulent diffusion. Our focus is upon the issue as to whether the route to fully developed turbulence in the stratified mixing layer is in any significant way determinant of diapycnal mixing efficiency as represented by an effective turbulent diffusivity. We characterize different routes to fully developed turbulence by the nature of the secondary instabilities through which a primary Kelvin–Helmholtz billow executes the transition to this state. We then demonstrate that different mechanisms of turbulence transition characterized in these different transition mechanisms lead to considerably different values for the efficiency of diapycnal mixing and also for the effective vertical flux of buoyancy. We show that the widely employed value of 0.15–0.2 for the efficiency of mixing in shear-induced stratified turbulence based upon both laboratory measurements and similarly low-Reynolds-number numerical simulations may be too low for the high-Reynolds-number regime characteristic of geophysical flows. Our results show that the mixing efficiency tends to a value of approximately 1/3 for sufficiently large Reynolds number at an intermediate value of 0.12 for the Richardson number. This is in agreement with a theoretical predictions of Caulfield, Tang and Plasting (*J. Fluid Mech.*, vol. 498, 2004, pp. 315–332) for the asymptotic value of mixing efficiency in stratified Couette flows. In the high-Reynolds-number regime, mixing efficiency is shown to vary over a considerable range during the course of a particular shear-induced mixing event. We explain this variation on the basis of a detailed examination of the underlying dynamics. Since values in the range 0.15–0.2 for mixing efficiency have been extensively employed to infer an effective diffusivity from ocean microstructure measurements and also in energy balance analyses of the requirements of the global ocean circulation, our findings have potentially important implications for large-scale ocean modelling. We also quantify the errors introduced by employing the Osborn (*J. Phys. Oceanogr.*, vol. 10, 1980, pp. 83–89) formula along with an efficiency of 0.15 to infer values for effective diffusivity, and explain the logical underpinnings of this conclusion. One of the more important aspects of this work from the perspective of our theoretical understanding of stratified turbulence is the demonstration that the inverse cascade of energy, which is facilitated by the vortex-merging process that is typical of laboratory experiments and of the low-Reynolds-number simulations of shear flow evolution, is strongly suppressed by increase of the Reynolds number to values typical of geophysical flows. Based on this finding, the application of results based on low-Reynolds-number (numerical or

† Email address for correspondence: amashaye@atmosp.physics.utoronto.ca

laboratory) experiments to high-Reynolds-number geophysical shear flows needs to be reconsidered.

Key words: shear layer turbulence, stratified turbulence, turbulent mixing

---

1. Introduction

The investigation of the mechanisms responsible for the transition of either stratified or unstratified shear flows to turbulence can be considered one of the classical problems of theoretical fluid mechanics. Kelvin–Helmholtz (KH) instability (Helmholtz 1868; Kelvin 1871), which is perhaps the best-studied and understood primary shear instability, has been the subject of increasingly detailed analysis over the past several years using theoretical methods, laboratory experiments, observational techniques and more recently high-resolution numerical simulations. From a practical point of view, the study of shear-induced turbulence in mixing layers has applications to the understanding of the mixing and transport of a variety of tracers in the atmosphere (Gossard 1990; Luce *et al.* 2010; Fukao *et al.* 2011) and for the understanding of the transport of heat, salt, sediment and other tracers at a wide range of scales in oceanic environments such as estuarine shear zones (Geyer *et al.* 2010), the deep ocean (van Haren & Gostiaux 2010), the oceanic thermocline (Thorpe 2005) and in oceanic density current overflows (Legg 2009).

Since shear instabilities may generate waves with wavelengths spanning a wide range, this mechanism may play a leading role in the cascade of energy from large-scale structures (such as barotropic or baroclinic eddies, internal tide-induced internal waves or internal solitary waves) to the smallest scales at which momentum is eventually dissipated due to viscous effects (Ley & Peltier 1978; Sutherland, Caulfield & Peltier 1994; Sutherland & Peltier 1994; Smyth & Peltier 1994; Moum *et al.* 2003; Nikurashin & Legg 2011). Recent developments in measurement techniques have enabled higher-resolution observations of density and velocity fields in the ocean and have made clear the ubiquitous occurrence of intense shear instabilities in this geophysical fluid (Geyer *et al.* 2010; van Haren & Gostiaux 2010). Of particular interest to us, and the primary motivation for the present work, are the mechanisms responsible for enhanced mixing in the abyssal ocean. We choose shear instability as a prototype example of such mechanisms, and attempt to answer several fundamental questions concerning shear-induced deep ocean mixing by detailed examination of the turbulence engendered by this mechanism. Our focus will be upon density stratified KH instability in particular as the abyssal ocean is stably stratified and the onset of turbulence is often mediated through the excitation of internal inertial waves (the so-called internal tide) excited by the flow over ocean bottom topography of the barotropic tide (Aucan *et al.* 2006; Griffiths & Peltier 2009; Nikurashin & Legg 2011; Salehipour *et al.* 2013).

Recently van Haren & Gostiaux (2012) have studied the mechanisms responsible for the generation of turbulence and vertical mixing above a seamount by means of moored temperature sensor measurements. They found ubiquitous 'finger-like' structures associated with shear instability (KH instability in this case, see van Haren & Gostiaux (2010)) that continuously contributed to the mixing of deep-water stratification during the down-slope tidal phase. Haren and Gostiaux calculated an effective coefficient for vertical diffusion across regions of high shear at the

crests and troughs of low-frequency internal-tide-induced internal waves, and found values an order of magnitude higher than those associated with the upper ocean as determined on the basis of tracer release experiments (Polzin *et al.* 1997; Ledwell *et al.* 2000). Haren and Gostiaux demonstrated that shear instability is indeed one of the mechanisms responsible for enhanced abyssal mixing (as has also been suggested by other studies such as Aucan *et al.* (2006), Gemmrich & van Haren (2001) and Nikurashin & Legg (2011)), and it is on this observational basis that we consider it the prototypical model problem for our purposes in the present paper. This mechanism is an oceanographic analogue of the mechanism of turbulence generation in the atmosphere by the breaking of internal waves above their topographic source of excitation (Peltier & Clark 1979) and subsequently in the lee of topography through KH instability of the jet that forms in the downslope region (Peltier & Scinocca 1990).

It is well known that, from a globally averaged perspective, the upwelling of abyssal waters is required to balance the formation of deep waters in both the North Atlantic and in the Southern Ocean. In the more traditional view of the meridional overturning circulation of the oceans, it has been assumed that the upwelling of abyssal waters is primarily due to enhanced diapycnal mixing in the ocean interior (Munk 1966; Munk & Wunsch 1998). Estimates obtained on this basis for the turbulent diffusivity required in the ocean interior and abyss to facilitate the upwelling are found to be on the order of $\kappa_v \sim 10^{-4}$ (m^2 s^{-1}). The results of these early analyses have motivated a large body of work dedicated to the estimation of κ_v as a function of depth in the oceanic interior. Most such studies have indeed led to estimates of $\kappa_v \sim 10^{-4}$ (m^2 s^{-1}) in the abyss but to lower values of $\kappa_v \sim 10^{-5}$ (m^2 s^{-1}) in the upper ocean thermocline region (Ledwell, Watson & Law 1993, 1998). Recent progress in understanding of the dynamics of the Southern Ocean, however, has revealed an alternative mechanism that could be responsible for the upwelling of deep waters (primarily of North Atlantic Deep Water (NADW)) to the surface, namely that due to the influence of the wind-driven surface mixed layer (Marshall & Speer 2012). In view of this inference, enhanced diapycnal mixing in the ocean need not be occurring throughout the ocean interior, and may be restricted to governing the upwelling of densest waters in the abyssal ocean (Wunsch & Ferrari 2004). In most studies which have attempted to close the oceanic overturning circulation through energy balance analyses or by employing thermodynamics-based approaches (Laurent & Simmons 2006) it has been assumed that the upward buoyancy flux can be related to the rate of dissipation of energy through a constant referred to as the 'mixing efficiency', denoted by $\mathscr{E}$ (Osborn 1980; Peltier & Caulfield 2003). For a turbulent flow in which the vertical buoyancy flux is primarily facilitated through turbulent mixing, $\mathscr{E}$ is almost the same as the flux Richardson number R_f, a parameter widely used in the oceanographic literature. Here $\mathscr{E}$ (or R_f) can be employed to relate the background stratification and energy dissipation to a value for the effective turbulent diffusivity κ_v through a relation first proposed by Osborn (1980) in the form of

$$\kappa_v = \frac{\mathscr{E}}{1 - \mathscr{E}} \frac{\mathscr{D}}{N^2}, \tag{1.1}$$

where N is the mean buoyancy frequency and $\mathscr{D}$ is the energy dissipation rate (both to be defined in what follows). This relation has been widely used to infer estimates of effective diffusivity at various ocean depths (see Thorpe (2005) for a review), to parametrize internal wave-induced mixing in the abyssal ocean (Jayne & Laurent 2001; Laurent, Simmons & Jayne 2002) and to parametrize shear mixing in oceanic overflows (Legg 2009). The popularity of (1.1) is mostly due to its simplicity and

to the fact that the rate of energy dissipation can be related to various measurable quantities using available measurement techniques. It needs to be noted that often in the literature, $\mathscr{E}/(1 - \mathscr{E})$ is mistakenly referred to as mixing efficiency $\mathscr{E}$ and a value of 0.2 is used for it, while Osborn (1980) proposed an upper bound of 0.15 for R_f (corresponding to $\mathscr{E}/(1 - \mathscr{E}) \sim 0.2$). The 'universal' value of 0.2 has been persistently used over the past decades to infer values for the effective diffusivity. More importantly, this canonical value has been widely used to obtain estimates of the mechanical energy needed to power the abyssal mixing required to maintain the observed overturning circulation of the oceans. If it were to prove necessary to employ a different value (such as 0.1 or 0.3), this would have significant potential implications for our understanding of this fundamental issue. Despite the general acceptance of values in the range 0.15–0.2 for mixing efficiency, our analyses, to be discussed in detail below, suggest that this assumption is not well-justified. In fact, there exists both observational and theoretical evidence that the efficiency may be either smaller or larger than 0.2 (the allowed deviations based upon analyses of the canonical shear instability model being in excess of 50 %) and that the actual value is expected to depend on the background stratification and may also depend on the anisotropy in the medium (see Thorpe (2005) for references). Thus, the accuracy with which κ_v is calculated from measurements is determined by the value employed for mixing efficiency as long as the concept of mixing efficiency is employed as a basis for determining the diffusivity.

In the present paper our intention is to study in detail, the process of transition to turbulence of a density stratified laminar shear flow, and the properties of the turbulent phase of the flow, such as the efficiency of mixing, isotropy of the turbulence thereby produced and the resulting turbulent cascade of energy. Moreover, as a theoretical counterpart to the many observation-based studies of diapycnal mixing in the abyssal ocean, we intend to test the accuracy of the assumption that $\mathscr{E} = 0.15$ and the applicability of the widely used formula (1.1) by means of numerical experiments. We consider KH instability to be the canonical example of primary shear instability. This choice is motivated by the abundance of observational evidence of its occurrence in the deep ocean and also in the oceanic thermocline. However, it is important to note that other primary shear instabilities (or hybrid modes) may emerge in shear layers (Carpenter, Balmforth & Lawrence 2010a; Balmforth, Roy & Caulfield 2012). The questions we attempt to answer and the general conclusions to which we are led will not be specific to KH instability and we expect our main conclusions to be of relevance to stratified turbulence in the oceanic environments in which the primary source of energy in turbulence is from shear and not convection.

After providing the appropriate theoretical background and introducing the numerical methodology used for conducting and analysing our numerical experiments (§§ 2.1–2.3), we begin our analyses by examination of the transition to turbulence of a primary shear instability generated billow through a series of secondary instabilities and explain the differences in turbulence characteristics of the mixing layers in terms of underlying dynamical processes rather than only in terms of the background flow parameters (§ 3). In this process we build upon our previous work, namely that of Mashayek & Peltier (2012a,b), in which non-separable linear stability analyses were employed to introduce a number of newly discovered secondary modes of instability which facilitate turbulent collapse of the primary KH billow. A lexicon of the most prominent instabilities found in these previous analyses is provided in appendix A. The difference between Mashayek & Peltier (2012a,b) and similar previous studies was in the relatively high Reynolds numbers considered in the

analyses, which has led to a number of new findings. In this article, we will be discussing a suite of high-resolution fully resolved numerical simulations of mixing in free density stratified parallel shear layers that cover a wide range of values of the governing non-dimensional parameters. Our first goal is to verify through these direct numerical simulation (DNS)-based analyses the theoretical findings of Mashayek & Peltier (2012*a*,*b*) concerning the operative transition mechanisms. Second, we intend to isolate the contribution of each of the secondary instabilities discussed in Mashayek & Peltier (2012*a*,*b*) to turbulent collapse of the shear layer and in doing so we will examine the validity of assumptions made in the derivation of the correlations employed as basis for the estimates of eddy diffusivities. Once the dynamics of transition to turbulence are explained, we turn our attention to the primary goal of this article which is to quantitatively evaluate the influence of 'route to turbulence' on turbulence characteristics such as mixing properties and the effective vertical diffusion of buoyancy (§ 4). The numerical experiments discussed in this work are special in the sense that they are conducted at sufficiently large Reynolds numbers (to be defined) that allow for the appearance of new physical processes which have not been reported in previous numerical studies (such as Cortesi, Yadigaroglu & Bannerjee 1998; Caulfield & Peltier 2000; Staquet 2000; Smyth, Moum & Caldwell 2001; Smyth 2003; Pham & Sarkar 2010) or previous laboratory experiments (for a review see Thorpe 2005). Our work should be viewed as directed to closing the gap between the properties of the low-Reynolds-number flows (typical of laboratory experiments and the existing body of numerical simulations) and those of geophysical flows. As briefly discussed by Mashayek & Peltier (2011*a*), there seems to be a characteristic difference between low-Reynolds-number flows and high-Reynolds-number flows in terms of both the transition to turbulence as well as the subsequent cascade of energy, and the related properties of the turbulence itself. A most important outcome of this work is to question the applicability of the results of laboratory experiments and the related body of computational work to the problem of the parametrization of the influence of turbulent mixing in geophysically realistic shear flows. The buoyancy Reynolds numbers (to be defined) corresponding to cases considered in this study are in the range of 10^2–10^3, which is considerably higher than most of previous DNSs of shear-induced turbulence. As will be discussed, this range is well within the range of buoyancy Reynolds number associated with oceanic flows.

2. Theoretical preliminaries

2.1. *Governing equations*

We study the temporal evolution of a stably stratified shear layer which is horizontally periodic in space. The initial background profiles of velocity and density are assumed to be of the form

$$\bar{U}^*(z^*) = U_0 \tanh\left(\frac{z^*}{h}\right), \tag{2.1}$$

$$\bar{\rho}^*(z^*) = \rho_a - \rho_0 \tanh\left(\frac{Rz^*}{h}\right), \tag{2.2}$$

where U_0 and ρ_0 are reference velocity and density, h is half the shear layer thickness, and R is the ratio of the characteristic scale of velocity variation to that of the density variation. The flow domain is described in Cartesian coordinates with x and z denoting the streamwise and vertical directions, respectively. It is well known (e.g. Drazin & Reid 1981) that an infinitely extended stratified shear layer is most unstable to KH
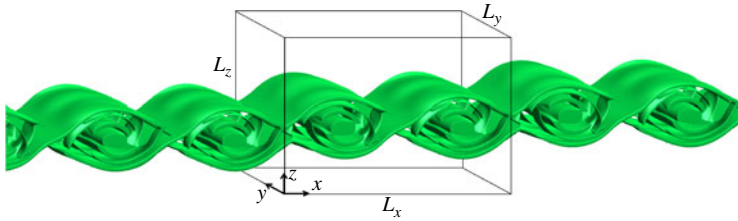
FIGURE 1. (Colour online) Schematic view of the computational domain.

instability if the gradient Richardson number defined by

$$Ri(z^*) = N^2/(shear)^2 = \frac{-g}{\rho_0}\frac{\partial \rho^*}{\partial z^*} \bigg/ \left(\frac{\mathrm{d}\bar{U}^*}{\mathrm{d}z^*}\right)^2 \tag{2.3}$$

is sufficiently small (smaller than $1/4$ for stratified flows (Miles 1961; Howard 1961)). For the velocity and density profiles considered here, the gradient Richardson number is a minimum at the centre of the shear layer. We consider this mid-layer value, which we refer to as Ri_0, as a measure of the strength of the stratification in the layer. The growth of the primary KH instability provides a background for growth of the secondary instability(s) responsible for the ultimate breakdown of the flow to turbulence.

The equations of motion, continuity (incompressibility in the Boussinesq limit) and energy conservation in dimensionless form are

$$\frac{\mathrm{D}u_i}{\mathrm{D}t} = -\frac{\partial p}{\partial x_i} - \frac{Ri_0}{R}\rho\delta_{i2} + \frac{1}{Re}\frac{\partial^2 u_i}{\partial x_j^2}, \tag{2.4}$$

$$\frac{\partial u_i}{\partial x_i} = 0, \tag{2.5}$$

$$\frac{\mathrm{D}\rho}{\mathrm{D}t} = \frac{1}{Re\,Pr}\frac{\partial^2 \rho}{\partial x_j^2}, \tag{2.6}$$

where $(i, j = 1, 2, 3)$. Our non-dimensionalization involves the following choices for the scales of time, distance, velocity, pressure and density, respectively

$$t = t^*U_0/h, \quad x_i = x_i^*/h, \quad u_i = u_i^*/U_0, \quad p = p^*/\rho_0 U_0^2, \quad \rho = \rho^*/\rho_0 \tag{2.7}$$

where ρ^* and p^* are departures from hydrostatic balance. It is also assumed that the Boussinesq approximation is valid. The governing equations will be numerically integrated using a pseudo-spectral numerical methodology which we employ to provide DNSs of the evolution equations which are spatially and temporally resolved so as to ensure that all relevant scales of motion are accurately represented. Figure 1 provides a schematic view of the computational domain. The streamwise (along shear) extent of the domain is set to be equal to two wavelengths of primary KH instability (based on linear stability theory). By enforcing periodic boundary conditions in the streamwise (x) and spanwise (y) directions, it is assumed that the flow field within the computational domain represents the dynamics in an almost periodic and effectively infinitely long wave train of KH billows (similar to those observed in titled tube experiments and recent observations). The choice of two wavelengths for the streamwise length of the domain is made to accommodate the vortex pairing instability, which is the fastest growing of the complete set of vortex amalgamation

instabilities (Klaassen & Peltier 1989)). The vertical extent of the computational domain has been chosen to be $L_z = 30\,h$. This is sufficiently large to ensure that the flow remains unaffected by the horizontal boundaries even in cases in which pairing occurs. The spanwise wavelength of the domain (L_y) has been chosen adaptively for each numerical simulation in such a way as to ensure that doubling of L_y does not impact the spanwise scales of the secondary instabilities that are able to grow on the primary KH wave. This adaptive approach is required to enable (from a computational cost perspective) longtime integration of the equations of motion from the initial laminar stage of shear layer evolution through to the turbulent collapse stage and the subsequent relaminarization.

In this study, we consider cases in the range of $750 \leqslant Re \leqslant 10\,000$ where Re is the Reynolds number and is defined by $Re = U_0 h / \nu$ (ν being the kinematic viscosity). This range corresponds to $10 < Re_b < 150$ where Re_b is the buoyancy Reynolds number defined as $Re_b = \mathscr{D}/(\nu N^2)$. For most cases considered in this study, the minimum gradient Richardson number (which obtains at the centre of the shear layer) is fixed at 0.12. This value is sufficiently large to enable realization of the full suite of secondary instabilities discussed in Mashayek & Peltier (2012a,b) which characterize the turbulence transition in a stratified layer. Since our numerical experiments exploit the maximum computational resources available to us, considering higher stratification levels could come at the cost of a reduced range of Reynolds number. In this study, our primary focus is on the role of the Reynolds number. Although we will briefly comment on the role of stratification by comparing cases with $Ri_0 = 0.12$ and cases with $Ri_0 = 0.04$, we will postpone the full investigation of the role of stratification at high Ri_0 values to future work. For present purposes we will also keep the Prandtl number (defined as $Pr = \nu/\kappa$ where κ is the thermal diffusivity) constant and equal to unity. Therefore, our discussions will be most relevant to thermally stratified flows rather than to salt stratified flows in which $Pr \sim O(100)$. For a discussion of the role of Pr on secondary instability and mixing in KH billows see Mashayek & Peltier (2012a) and Mashayek & Peltier (2011b). The influence of this parameter on the evolution of initially two-dimensional KH billows has previously been discussed in Klaassen & Peltier (1985a). We will also assume $R = 1.1$ (Caulfield, Yoshida & Peltier 1996)) to avoid further complicating the parameter space over which our numerical experiments are conducted. It is important to note, however, that larger values of R along with $Ri_0 > 0.25$ might give rise to other primary instabilities such as Holmboe instability (Holmboe 1962; Smyth, Klaassen & Peltier 1988; Smyth & Peltier 1991; Carpenter, Lawrence & Smyth 2007; Carpenter *et al.* 2010b) or Taylor–Caulfield instability (Taylor 1931; Caulfield 1994). Note that while we have tried to be consistent with most of the existing literature concerning shear instabilities regarding the definition of Re, there are discrepancies in the literature in the way that Re is defined. Therefore, care must be taken in direct comparisons of our results with those of others. For example, our Reynolds numbers should be multiplied by two to obtain the values cited in the work of Smyth & Winters (2003), Smyth, Carpenter & Lawrence (2007), Pham, Brucker & Sarkarand (2009) and Pham & Sarkar (2010).

The simulations are initialized by addition of incompressible white noise to the velocity field and white noise with zero mean to the density field. This will ensure that none of the secondary instabilities is favoured over others. Free-slip impermeable boundary conditions on the velocity components are applied at the top and bottom boundaries of the domain, together with a condition of zero density flux. The validity of the numerical experiments will be examined using diagnostic equations which will be introduced in the next section. Moreover, as an independent test for validation

Re	Ri_0	Pr	L_x	L_y	L_z	N_x	N_y	N_z
750	0.04	1	28.56	4 and 8	30	320	64 and 128	600
750	0.085	1	28.56	4 and 8	30	320	64 and 128	600
750	0.12	1	28.56	4 and 8	30	512	96 and 192	800
1000	0.12	1	28.54	3.5 and 7	30	768	96 and 192	800
2000	0.12	1	28.54	3.5 and 7	30	768	96 and 192	800
4000	0.04	1	28.54	3	30	1024	128	1216
4000	0.12	1	28.54	3	30	1024	128	1216
6000	0.12	1	28.54	3	30	1024	128	1216
8000	0.12	1	28.54	3	30	1024	128	1216
10000	0.04	1	28.54	3	30	1280	160	1216
10000	0.12	1	28.54	3	30	1280	160	1216

TABLE 1. Details of the 3D numerical experiments.

of the numerical tools used in this work, results of Caulfield & Peltier (2000) (which were obtained using a different numerical toolbox) were reproduced prior to performing the numerical experiments that form the basis for analysis in this work. Table 1 provides the required information concerning the three-dimensional numerical experiments to be analysed in subsequent sections.

2.2. *Energetics*

To facilitate detailed analysis of the outcomes of the numerical simulations we employ analyses similar to Caulfield & Peltier (2000). We begin by averaging the 3D velocity field, $\boldsymbol{u}(x, y, z, t)$, on the horizontal xy plane so as to define the field

$$\bar{\boldsymbol{u}}(z) = \frac{1}{L_x L_y} \int_0^{L_x} \int_0^{L_y} \boldsymbol{u} \, dx \, dy. \tag{2.8}$$

The two-dimensional perturbation to this height-dependant horizontally averaged field can then be calculated by subtracting $\bar{\boldsymbol{u}}(z)$ and averaging in the spanwise direction:

$$\boldsymbol{u}_{2D} = \int_0^{L_y} [\boldsymbol{u} - \bar{\boldsymbol{u}}(z)] \, dy. \tag{2.9}$$

Here $\boldsymbol{u}_{2D}$ represents the velocity field associated with 2D perturbations such as the primary KH wave itself, 2D vortex merging and 2D secondary shear instability (SSI) of the braid (see Appendix for definitions and see Mashayek & Peltier (2012*a*) or Mashayek & Peltier (2012*b*) for further details). The velocity field associated with 3D perturbations can be calculated from the following definition

$$\boldsymbol{u}_{3D} = \boldsymbol{u} - \boldsymbol{u}_{2D} - \bar{\boldsymbol{u}}(z). \tag{2.10}$$

With the velocity properly decomposed into $\bar{\boldsymbol{u}}$, $\boldsymbol{u}_{2D}$ and $\boldsymbol{u}_{3D}$, the total kinetic energy of the flow ($\mathscr{K}$), the average kinetic energy of the mean background flow ($\bar{\mathscr{K}}$), the kinetic energy associated with the spanwise-averaged 2D perturbations ($\mathscr{K}_{2D}$) and the average kinetic energy of 3D perturbations ($\mathscr{K}_{3D}$) can be defined as

$$\mathscr{K}(t) = \bar{\mathscr{K}} + \mathscr{K}_{2D} + \mathscr{K}_{3D} = \frac{1}{L_x L_y L_z} \int_0^{L_x} \int_0^{L_y} \int_0^{L_z} [u^2 + v^2 + w^2] \, dz \, dy \, dx, \tag{2.11}$$

$$\bar{\mathscr{K}} = \frac{1}{L_z} \int_0^{L_z} \frac{\bar{\boldsymbol{u}}^2}{2} \, dz, \tag{2.12}$$

$$\mathcal{K}_{2D} = \frac{1}{L_x L_z} \int_0^{L_x} \int_0^{L_z} [u_{2D}^2 + w_{2D}^2] \, \mathrm{d}z \, \mathrm{d}x, \tag{2.13}$$

$$\mathcal{K}_{3D} = \frac{1}{L_x L_y L_z} \int_0^{L_x} \int_0^{L_y} \int_0^{L_z} [u_{3D}^2 + v_{3D}^2 + w_{3D}^2] \, \mathrm{d}z \, \mathrm{d}y \, \mathrm{d}x. \tag{2.14}$$

The evolution equation for the total kinetic energy can then be shown to be (Klaassen & Peltier 1985b)

$$\sigma = \frac{1}{2\mathcal{K}} \frac{\mathrm{d}}{\mathrm{d}t} \mathcal{K} = -\mathcal{H} - \mathcal{D}, \tag{2.15}$$

where $\mathcal{H}$ is the buoyancy flux defined by

$$\mathcal{H} = \frac{Ri_0}{2\mathcal{K} R} \frac{1}{L_x L_y L_z} \int_0^{L_x} \int_0^{L_y} \int_0^{L_z} (\rho w) \, \mathrm{d}z \, \mathrm{d}y \, \mathrm{d}x, \tag{2.16}$$

and $\mathcal{D}$ is the positive-definite viscous dissipation term defined by

$$\mathcal{D} = \frac{1}{2\mathcal{K} Re} \frac{1}{L_x L_y L_z} \int_0^{L_x} \int_0^{L_y} \int_0^{L_z} (\nabla \boldsymbol{u})^2 \, \mathrm{d}z \, \mathrm{d}y \, \mathrm{d}x. \tag{2.17}$$

According to (2.15), a positive buoyancy flux is at the cost of $\mathcal{K}$. Similarly, the dissipation term plays the role of a sink for the kinetic energy reservoir. Right- and left-hand sides of (2.15) can be calculated independent of each other and their difference can be treated as a measure of the accuracy of the numerical simulations. For all of the flows whose properties are listed in table 1 this difference was found *a posteriori* to be smaller than one part in a million.

An equation for the evolution of 3D perturbations can also shown to be of the form (Klaassen & Peltier 1985b)

$$\begin{aligned}
\sigma_{3D} &= \frac{1}{2\mathcal{K}_{3D}} \frac{\mathrm{d}}{\mathrm{d}t} \mathcal{K}_{3D} \\
&= \mathcal{R}_{3D} + \mathcal{S}h + \mathcal{A} - \mathcal{H}_{3D} - \mathcal{D}_{3D},
\end{aligned} \tag{2.18}$$

where the first term represents extraction of energy from the background mean shear by means of Reynolds stresses and is defined as

$$\mathcal{R}_{3D} = -\frac{1}{2\mathcal{K}_{3D}} \frac{1}{L_x L_y L_z} \times \int_0^{L_x} \int_0^{L_y} \int_0^{L_z} \left(u_{3D} w_{3D} \frac{\partial \bar{U}}{\partial z} \right) \, \mathrm{d}z \, \mathrm{d}y \, \mathrm{d}x, \tag{2.19}$$

the second term in (2.18) represents extraction of energy from the background KH billow and is given by

$$\mathcal{S}h_{3D} = -\frac{1}{2\mathcal{K}_{3D}} \frac{1}{L_x L_y L_z} \times \int_0^{L_x} \int_0^{L_y} \int_0^{L_z} \left(u_{3D}^2 \frac{\partial u_{kh}}{\partial x} + w_{3D}^2 \frac{\partial w_{kh}}{\partial z} \right) \, \mathrm{d}z \, \mathrm{d}y \, \mathrm{d}x, \tag{2.20}$$

the third term represents the stretching deformation of the 3D perturbation field and is defined as

$$\mathcal{A} = -\frac{1}{4\mathcal{K}_{3D}} \frac{1}{L_x L_y L_z} \times \int_0^{L_x} \int_0^{L_y} \int_0^{L_z} (u_{3D}^2 - w_{3D}^2) \left(\frac{\partial u_{2D}}{\partial x} - \frac{\partial w_{2D}}{\partial z} \right) \, \mathrm{d}z \, \mathrm{d}y \, \mathrm{d}x, \tag{2.21}$$

Finally $\mathcal{H}_{3D}$ and $\mathcal{D}_{3D}$ are the buoyancy flux and viscous dissipation terms associated with three-dimensional perturbations which are defined respectively as

$$\mathcal{H}_{3D} = \frac{Ri_0}{2\mathcal{K}_{3D}} \frac{1}{L_x L_y L_z} \times \int_0^{L_x} \int_0^{L_y} \int_0^{L_z} \rho_{3D} w_{3D} \, \mathrm{d}z \, \mathrm{d}y \, \mathrm{d}x, \tag{2.22}$$

$$\mathscr{D}_{3D} = \frac{1}{2Re\,\mathscr{K}_{3D}} \frac{1}{L_x L_y L_z} \times \int_0^{L_x} \int_0^{L_y} \int_0^{L_z} (\boldsymbol{\nabla u}_{3D})^2)\,\mathrm{d}z\,\mathrm{d}y\,\mathrm{d}x. \tag{2.23}$$

Similar to (2.15) and (2.18) can be used as a measure of the accuracy of the simulations, particularly during the turbulent phase of the flows. This can be exploited by comparing the left- and right-hand sides of (2.18) which can be independently calculated from simulation results. This is done in appendix B for two sample cases. For all cases of table 1 the right- and left-hand sides of (2.18) were found to be identical to within a tolerance of 0.001 %.

Following Caulfield & Peltier (2000) and Peltier & Caulfield (2003), the time rate of change of the total mechanical energy of the system under consideration, E, can be written as

$$\frac{\mathrm{d}E}{\mathrm{d}t} = \frac{\mathrm{d}\mathscr{K}}{\mathrm{d}t} + \frac{\mathrm{d}\mathscr{P}}{\mathrm{d}t}, \tag{2.24}$$

where $\mathscr{K}$ and $\mathscr{P}$ are the total kinetic and potential energies. The potential energy is defined as

$$\mathscr{P} = \frac{Ri_0}{R} \frac{1}{L_z} \times \int_0^{L_z} z\bar{\rho}\,\mathrm{d}z, \tag{2.25}$$

and the time rate of change of the potential energy can be written as

$$\frac{\mathrm{d}\mathscr{P}}{\mathrm{d}t} = \mathscr{H} + \mathscr{D}_p, \tag{2.26}$$

where $\mathscr{D}_p$, a strictly positive quantity, is the rate at which the potential energy of a statically stable and motionless density stratification would increase through conversion of internal energy to potential energy. In our computational procedure, this can be calculated from

$$\mathscr{D}_p = \frac{Ri_0(\rho_{bottom} - \rho_{top})}{L_z RePr}, \tag{2.27}$$

where ρ_{bottom} and ρ_{top} are the non-dimensional densities at the top and bottom boundaries of the domain. As will be clear from (2.15), the total kinetic energy of the system can be decreased through net upward motion of dense fluid (i.e. positive $\mathscr{H}$) which leads to an increase in the potential energy of the system as expressed by (2.26). Two mechanisms responsible for the loss of the total mechanical energy of the system to internal energy are the viscous dissipation ($\mathscr{D}$) and $\mathscr{D}_p$. In other words, combining (2.24), (2.15) and (2.26) gives

$$\frac{\mathrm{d}E}{\mathrm{d}t} = \mathscr{D} + \mathscr{D}_p, \tag{2.28}$$

where the right-hand side is negative-definite ($|\mathscr{D}| \gg |\mathscr{D}_p|$).

The potential energy itself can be divided into two parts namely the background potential energy, $\mathscr{P}_B$, defined as

$$\mathscr{P}_B = \frac{Ri_0}{R} \frac{1}{L_z} \times \int_0^{L_z} z\rho_B(z)\,\mathrm{d}z, \tag{2.29}$$

and the available potential energy, $\mathscr{P}_A$. In which case we may write

$$\mathscr{P} = \mathscr{P}_B + \mathscr{P}_A. \tag{2.30}$$

The background density profile $\rho_B(z)$ is associated with the minimum (background) potential energy of the system (Caulfield & Peltier 2000; Winters *et al.* 1995) and can

only be increased through irreversible mixing processes or by the diffusion term $\mathscr{D}_p$. By denoting the irreversible mixing by $\mathscr{M}$, we can write

$$\frac{\mathrm{d}\mathscr{P}_B}{\mathrm{d}t} = \mathscr{M} + \mathscr{D}_p. \tag{2.31}$$

Combining this with (2.26) and (2.30) we may therefore write

$$\frac{\mathrm{d}\mathscr{P}_A}{\mathrm{d}t} = \mathscr{H} - \mathscr{M} = \mathscr{S}. \tag{2.32}$$

The available potential energy is that part of the total potential energy which is 'available' to be converted back into kinetic energy. Hence, the right-hand side of (2.32), $\mathscr{S}$, simply represents the reversible stirring of the flow whereas the right-hand side of (2.31) represents irreversible mixing. Using the definitions of mixing and stirring, and by combining (2.15) and (2.32) we may therefore write

$$\frac{\mathrm{d}\mathscr{K}}{\mathrm{d}t} = -\mathscr{S} - \mathscr{M} + \mathscr{D}. \tag{2.33}$$

Equation (2.33) simply demonstrates that the kinetic energy can be changed through stirring of the fluid, irreversible mixing of the fluid or viscous dissipation. The first term on the right-hand side of (2.33) represents a reversible process whereas the remaining two terms represent irreversible processes. Therefore, an instantaneous mixing efficiency can be defined as the ratio of the rate at which kinetic energy is lost to mixing, and the rate at which it is lost to both mixing and dissipation:

$$\mathscr{E}_i = \frac{\mathscr{M}}{\mathscr{M} - \mathscr{D}}. \tag{2.34}$$

By definition, $\mathscr{E}_i$ is smaller than 1. Similar to Caulfield & Peltier 2000, the cumulative mixing efficiency (a quantity which can be used for comparison to experiments) is defined as

$$\mathscr{E}_c = \frac{\displaystyle\int_0^t \mathscr{M}(t')\,\mathrm{d}t'}{\displaystyle\int_0^t \mathscr{M}(t')\,\mathrm{d}t' - \int_0^t \mathscr{D}(t')\,\mathrm{d}t'}. \tag{2.35}$$

In the analyses which follow in the subsequent sections, we will further employ a 'post-transition cumulative' mixing efficiency, $\mathscr{E}_c^{3D}$ which is defined by

$$\mathscr{E}_c^{3D} = \frac{\displaystyle\int_{t_{3D}}^t \mathscr{M}(t')\,\mathrm{d}t'}{\displaystyle\int_{t_{3D}}^t \mathscr{M}(t')\,\mathrm{d}t' - \int_{t_{3D}}^t \mathscr{D}(t')\,\mathrm{d}t'}, \tag{2.36}$$

where t_{3D} is the time at which the 3D perturbations saturate and marks the onset of fully turbulent flow and so (2.36) represents the efficiency of mixing in the turbulent phase of flow evolution. As mentioned in the introduction, $\mathscr{E}_c^{3D} \approx R_f$ where R_f is the flux Richardson number.

2.3. *Spectral representation*

To compare the evolution of secondary instabilities in our simulations with predictions of the secondary stability analysis of Mashayek & Peltier (2012*a*,*b*), it is useful to

obtain spectral representations of the flow fields within particular intervals of time within each simulation. To do this, we employ the Fourier transform of the streamwise vorticity field, ω_x, to obtain a discrete spectral representation of the field as:

$$\omega_x(x, y, z, t) = \sum_{n=-N}^{N} c_n(d_n, x, z, t)e^{id_n y}, \tag{2.37}$$

where c_n are the Fourier coefficients defined by

$$c_n(d_n, x, z, t) = \frac{1}{L_y} \int_0^{L_y} \omega_x e^{-id_n y} \, dy, \tag{2.38}$$

and $d_n = 2\pi n/L_y$ is the spanwise wavenumber. The relative importance of various spectral components can be represented by the normalized spanwise power spectral density $P(d_n)$ defined as

$$P(d_n, t) \equiv \frac{\dfrac{1}{L_x L_z} \displaystyle\int_0^{L_x} \int_0^{L_z} |c_n(d_n, x, z)|^2 \, dz \, dx}{\displaystyle\sum_{n=0}^{N} \frac{1}{L_x L_z} \int_0^{L_x} \int_0^{L_z} |c_n(d_n, x, z)|^2 \, dz \, dx}. \tag{2.39}$$

As we are interested in the early stages of growth of secondary instabilities which originate inside the cores and on the braid of a KH billow, we perform such Fourier decompositions for the core region, the braid region, and the total flow field separately. The resolution employed for all three regions in our analyses is $N = 128$.

Furthermore, to rigorously test the prediction of Mashayek & Peltier (2012a) regarding suppression of an inverse cascade of energy through vortex pairing as a consequence of the emergence of a large number of rapidly growing three-dimensional instabilities at high Reynolds number, we perform a streamwise decomposition of the flow field. After spanwise-averaging of the 3D density field, we decompose the resulting 2D field as

$$\rho_{2D}(x, z, t) = \sum_{n=-M}^{M} a_n(b_n, z, t)e^{ib_n x}, \tag{2.40}$$

where the a_n are the Fourier coefficients and $b_n = 2\pi n/(2L_x)$ is the streamwise wavenumber. At any time of interest, the relative importance of various spectral components can be represented by the normalized streamwise power spectral density $P(b_n)$ defined as

$$P(b_n, t) \equiv \frac{\dfrac{1}{L_z} \displaystyle\int_0^{L_z} |a_n(b_n, z)|^2 \, dz}{\displaystyle\sum_{n=0}^{M} \frac{1}{L_z} \int_0^{L_z} |a_n(b_n, z)|^2 \, dz}. \tag{2.41}$$

By choosing the streamwise domain extent to be $2L_x$ for Fourier decomposition, wave one will correspond to the pairing mode and wave two to the primary KH wave. We employ the resolution $M = 512$ for this series of calculations.
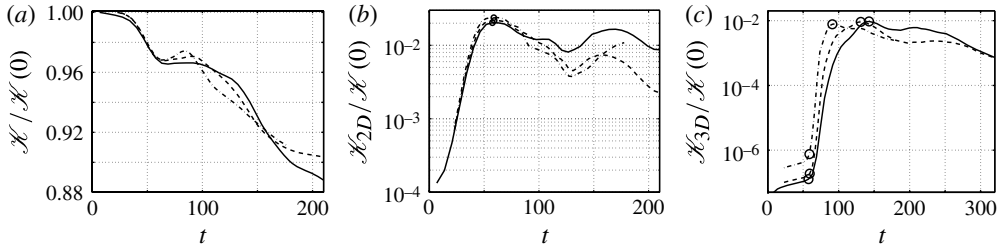
FIGURE 2. Time evolution of $\mathcal{K}/\mathcal{K}(0)$ in (a), $\mathcal{K}_{2D}/\mathcal{K}(0)$ in (b) and $\mathcal{K}_{3D}/\mathcal{K}(0)$ in (c) for $Re = 750$ (solid lines), $Re = 1000$ (dashed line) and $Re = 2000$ (dashed-dotted line). Circles in (b) correspond to t_{2D}. Two circles on each curve in (c) correspond to t_{2D} and t_{3D}, respectively.

3. The influence of Reynolds number

As discussed briefly in Mashayek & Peltier (2011b), there appears to be a change in characteristic properties of a mixing layer once the Reynolds number is increased so as to be sufficiently in excess (the exact value depending on Pr as discussed in Mashayek & Peltier (2011b)) of those typically achieved in laboratory experiments. This change is associated with the emergence of a 'zoo' of secondary instabilities (as described in Mashayek & Peltier (2012a,b)) which exist at high Re, some of the inhabitants of which have not been observed in laboratory experiments but which were expected to be observed in geophysical shear layers. We will therefore divide the cases to be discussed in this section into 'low-Reynolds-number' and 'high-Reynolds-number' groups. To focus on the role of Re, we will also keep Ri_0 and Pr constant at 0.12 and 1, respectively, for the purpose of the initial analyses to be discussed in this paper. The influence of Ri_0 will be discussed in the subsequent section whereas the cumulative influence of all three parameters will be discussed in the penultimate section.

3.1. *The low-Reynolds-number regime*

In this subsection we analyse three different cases with $Re = 750$, 1000 and 2000. Figure 2 shows plots of the time evolution of the normalized total kinetic energy ($\mathcal{K}$), the normalized kinetic energy associated with the primary KH wave ($\mathcal{K}_{2D}$) and the normalized kinetic energy associated with three-dimensional perturbations ($\mathcal{K}_{3D}$) for all three Reynolds numbers. In each case, the growth of the primary KH billow is at the expense of the background kinetic energy. We refer to the time at which the KH wave reaches its maximum kinetic energy as t_{2D} (shown by circles on curves in the middle panel). At approximately the same time as t_{2D}, three-dimensional perturbations begin to grow. As discussed in Mashayek & Peltier (2012b), 3D perturbations extract their energy primarily from the primary KH billow (note the near-flat $\mathcal{K}$ curves and the sloping $\mathcal{K}_{2D}$ curves between $t = 60$ and $t = 100$). At a time which we refer to as t_{3D}, and which is shown by circles on the curves in figure 2(c), 3D perturbations saturate and this marks the onset of the fully turbulent phase of flow evolution. The noticeably short time between t_{2D} and t_{3D} is the transition phase, in which a number of 2D and 3D instabilities emerge on the mostly 2D background KH wave, interact and break down the flow into turbulence.

A comparison between the three cases shown in the figure demonstrates that an increase in Re does not influence the growth of the primary KH wave significantly. This is expected as the growth rate of the primary wave is mainly a function of the
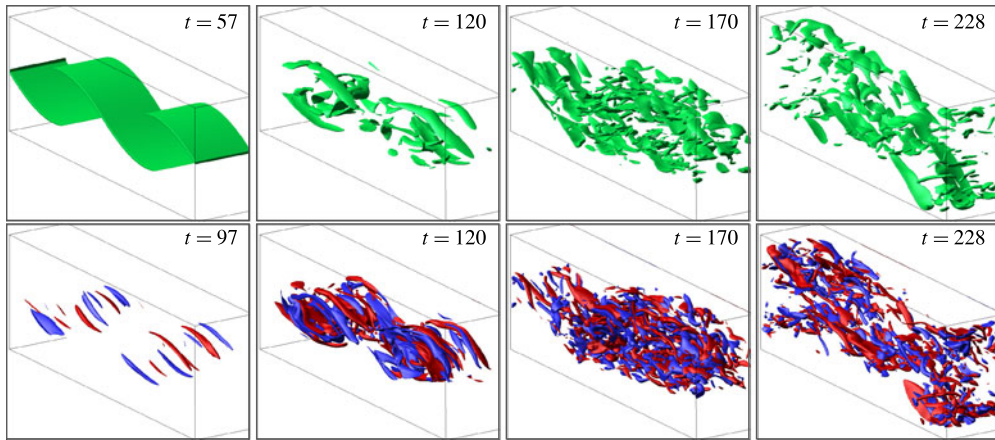
FIGURE 3. Spanwise vorticity isosurface (green) of $\omega_y = 0.72$ in top row and streamwise vorticity isosurfaces of $\omega_x = 0.2$ (red) and $\omega_x = -0.2$ (blue) in bottom row for $Re = 750$, $Ri_0 = 0.12$ and $Pr = 1$ ($t_{2D} = 58$ and $t_{3D} = 143$). Note that the boxes enclosing the KH billows do not represent the computational domain. For dimensions of the computational domain see table 1.
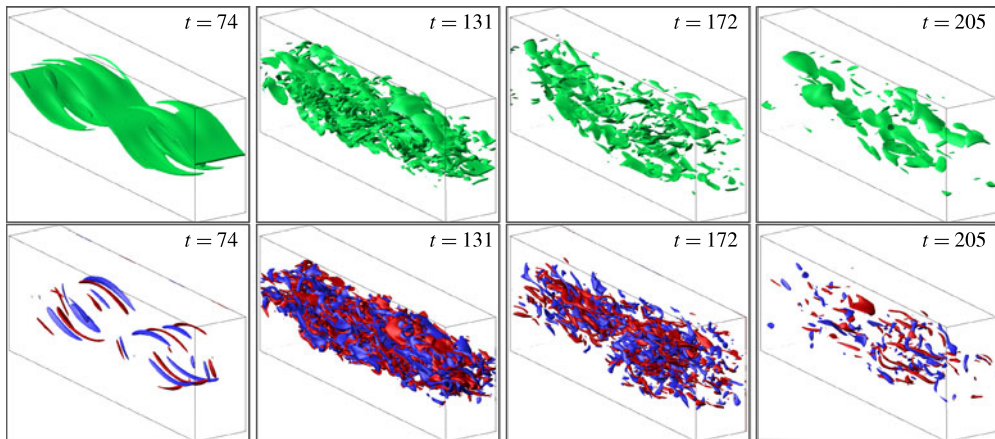

FIGURE 4. Same as figure 3 but for $Re = 1000$, $Ri_0 = 0.12$ and $Pr = 1$ ($t_{2D} = 60$ and $t_{3D} = 131$).

background stratification (see Mashayek & Peltier (2012a) and Corcos & Sherman (1976) for details). The growth of 3D instabilities, however, is influenced by the increase in Re (as expected based on the stability analyses of Mashayek & Peltier (2012a,b)). Figure 2(c) shows that with increase in Re, 3D perturbations emerge earlier and grow faster, causing the transition time window to contract.

Figures 3 and 4 show plots of vorticity isosurfaces for the $Re = 750$ and 1000 cases at various times during flow evolution. Owing to the great similarity between the $Re = 1000$ and 2000 cases, vorticity plots for the latter case are not presented. The first column in each figure illustrates the stages of emergence of the secondary convective instability (SCI) in the cores of the KH billows, the mode of instability first

identified in the analyses of Klaassen & Peltier (1985*b*). The subsequent panels in the figures show evolution of the SCI-induced convective rolls which are aligned with the background shear. The interaction between these rolls leads to higher-order instabilities and ultimately breakdown of the flow into turbulence.

Panels corresponding to times $t = 170$ and 228 in figure 3 reveal an upscale cascade (doubling of the wavelength) of energy from the scale of the primary KH wave. This is a somewhat suppressed form of the pairing instability. Although this is difficult to observe in the vorticity plots, it can be detected in the $\mathcal{K}_{2D}$ plot in figure 2 in the form of a rapid increase in $\mathcal{K}_{2D}$ at the expense of both $\mathcal{K}$ and $\mathcal{K}_{3D}$. The same behaviour is observed at $Re = 1000$ and 2000 in figure 2. It should be noted that this upscale turbulent cascade is already somewhat different from the pairing instability observed frequently in two-dimensional simulations of KH waves, or of 3D simulations at even lower Reynolds numbers. In two-dimensional (or low Re) pairing, vortex cores orbit each other and thereby contribute greatly to preturbulent vertical mixing, and extract significant amounts of energy from the background flow and from smaller perturbations. As shown in Mashayek & Peltier (2012*b*), preturbulent pairing prohibits various secondary instabilities from growing by draining their source of kinetic energy. The turbulent-phase pairing illustrated in figures 3 and 4 on the other hand has a mild effect on the energy budgets of other 3D perturbations, and occurs in the already turbulent phase of the flow, and thus assists the relaminarization process rather than the transition to turbulence. It is well-known that the pairing instability is suppressed by an increase in background stratification due to suppression of vertical motion. However, a rather new result, and one which was briefly discussed in Mashayek & Peltier (2011*b*), is that at sufficiently high Reynolds numbers, early emergence and rapid growth of a number of 3D secondary instabilities destroy the coherence of the large-scale structure of the primary KH wave, thereby preventing pairing from occurring. This was conjectured by Mashayek & Peltier (2012*b*) and will be verified in the subsequent section when we discuss the high-Re cases.

We are now in a position to make quantitative comparisons between results of our 3D numerical simulations and the non-separable linear stability analyses of Mashayek & Peltier (2012*a*). To do so, we include two plots from that study in figure 5 for a case with $Re = 1000$, $Pr = 1$ and $Ri_0 = 0.12$. Figure 5(*a*) compares growth rates of various modes of secondary instability which could conceivably grow on the background KH wave. Note that the analyses in Mashayek & Peltier (2012*a*) are frozen-in time analyses, meaning that at each time, it is assumed that the background KH wave evolves much more slowly than the amplifying secondary modes. This assumption is well-justified in this context due to the existence of a clear separation of time scales as discussed in Mashayek & Peltier (2012*a*). Figure 5(*a*) should be interpreted as follows: at each specific time, the instability with the largest growth rate has the highest probability of emerging in the flow. Therefore, during the transition period, SCI and stagnation point instability (SPI) have the highest probability of emerging, while the probability of occurrence of SSI of the braid decreases with time (because of the increase in the rate of velocity strain at the stagnation point due to growth of the KH vortex cores), and pairing instability remains active but only weakly so. As demonstrated previously in the 3D simulations illustrated in figure 3, SCI indeed emerges as the dominant mode of instability, and the pairing instability manifests itself only weakly and only in the turbulent phase of the flow. Less obvious in figure 3 is that SPI also emerges, although briefly, in flow evolution of the $Re = 1000$ case. To illustrate this, we plot spanwise vorticity on a slice passing through the middle of the domain for $Re = 1000$ and also for $Re = 2000$ in figure 6.
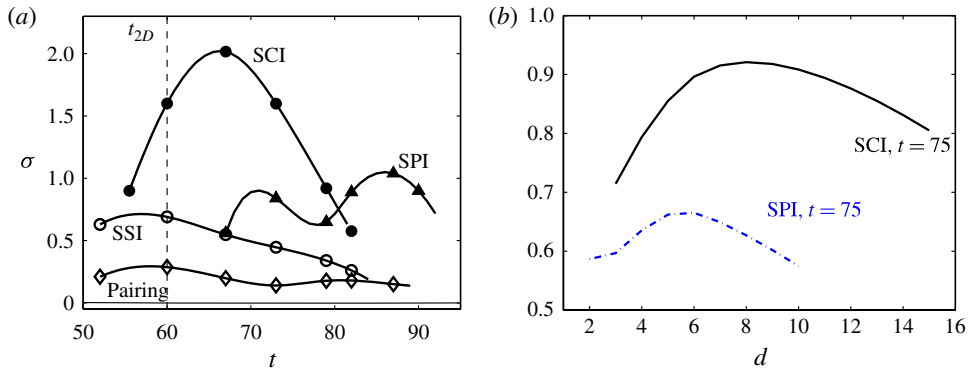
FIGURE 5. (Colour online) (*a*) The results of the stability analysis for fastest growing mode of various instabilities (see appendix A for a view of instability types) during evolution of case $Re = 1000$, $Ri_0 = 0.12$ and $Pr = 1$: the solid curve with filled circles for SCI with $d = 8.5$, the solid line with open circles for SSI with $d = 0$, the solid line with diamonds for the pairing instability and the solid line with filled triangles for SPI with $d = 7$. The symbols show the actual data points for which the analysis has been done while the lines are spline fits. The vertical dashed lines shows t_{2D}. (*b*) Growth rate versus spanwise wavenumber, d, for the SPI mode (dashed-dotted line) and the SCI mode (solid line) both at $t = 75$.
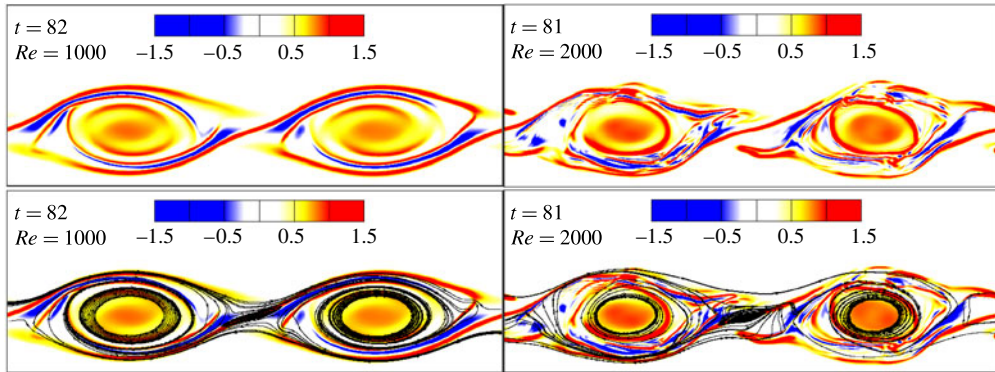
FIGURE 6. Contour plots (with and without streamlines overlain) of ω_z on the $y = L_y/2$ plane for a time before SCI-induced turbulent collapse of the billow for $Re = 1000$ (left column) and $Re = 2000$ (right column).

Streamlines are also included in the figure to show the formation of a recirculating region (characteristic of the SVBI–SPI family of instabilities) at the stagnation point of the train of KH billows. Although this mode does not survive the turbulent collapse of the billow for $Re = 1000$ or 2000, comparison between the two cases in figure 6 shows that increase in Re promotes this mode. It will be shown that for higher Reynolds numbers, SPI plays an important role in transition to turbulence of the mixing layer.

All of the secondary instabilities for which results are presented in figure 5(*a*) exist over a range of spanwise wavenumbers, denoted by d. While SSI and pairing have their fastest growth rates for $d = 0$ (i.e. when they are 2D), SCI and SPI are highly 3D. Figure 5(*b*) shows plots of growth rate versus wavenumber for the two instabilities
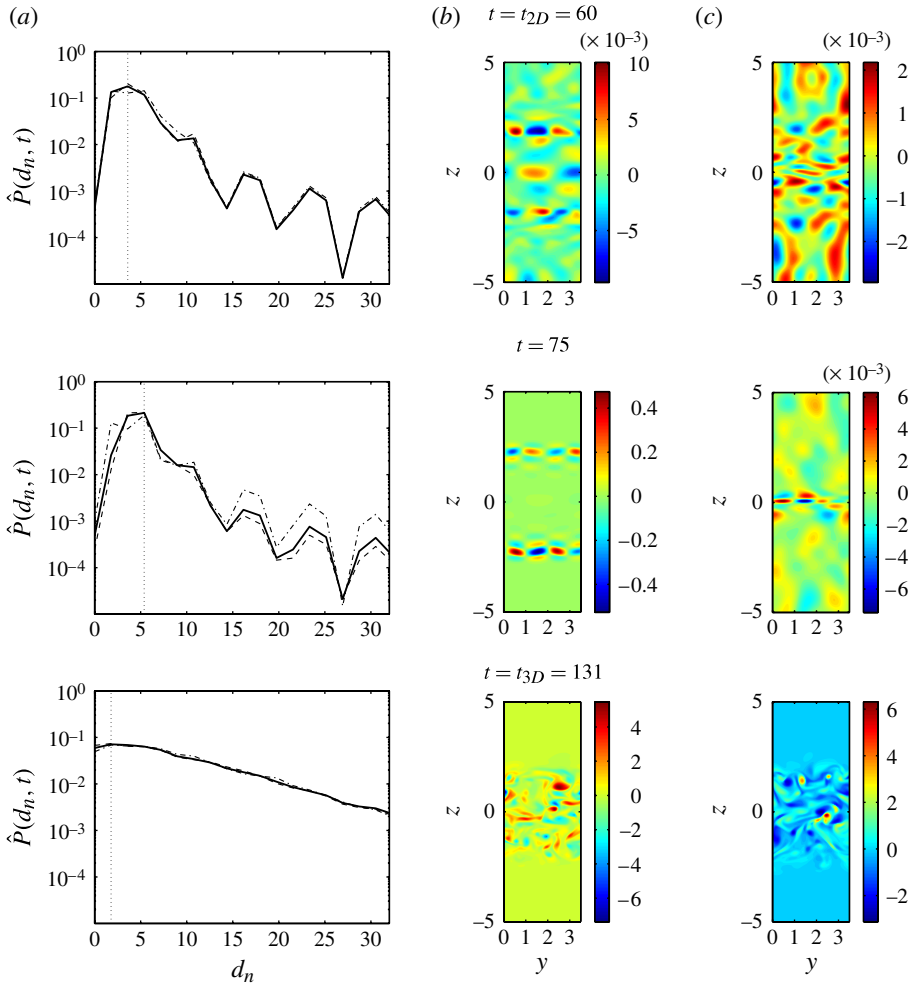
FIGURE 7. Case $Re = 1000$, $Ri_0 = 0.12$: variation of various components (total in solid line, core in dashed line and braid in dashed-dotted line) of PSD $\hat{P}(d_n, t)$ against the spanwise wavenumber d_n in left column and streamwise vorticity (ω_x) contours on a plane normal to the x-axis and passing through the centre of the core (b,e,h) and on a plane normal to the x-axis and passing through the braid stagnation point (c,f,i). The first and third rows correspond to $t = t_{2D} = 60$ and $t = t_{3D} = 131$, respectively, and the middle row corresponds to $t = 74$ which is a time between t_{2D} and t_{3D}. Times t_{2D} and t_{3D} are shown in figure 2 with circles.

which have the highest probability of emerging according to figure 5(a), namely the SCI and the SPI modes. Both curves correspond to a time $t = 75$ which is a time within the transition period (i.e. between t_{2D} and t_{3D}). Both instabilities seem to be fastest growing at $d \sim 5$–6, with the spanwise wavenumber for SPI and its growth rate being slightly smaller than those of the SCI. The left column of figure 7 shows plots of the spanwise-averaged power spectral density (PSD) of streamwise vorticity at three different times spanning the transition period for $Re = 1000$. Each plot in the left column includes three curves, one for the spectrum averaged over the vortex core region (dashed line), one for the braid region (dashed-dotted line) and one for

the total KH billow (solid line). The other two columns of the figure also show filled contour plots of the streamwise vorticity on a plane passing through the middle of the core (middle column) and on a plane passing through the braid stagnation point (right column). The first row of the plot corresponds to t_{2D} and illustrates the early stages of formation of secondary instabilities (note the difference in colourbar values from the first to the second and third rows). By time $t = 75$ in the middle row, SCI has fully evolved in the vorticity layers inside the vortex core with a spanwise wavenumber of $d \sim 5.5$, in excellent agreement with the theoretical prediction of figure 5(*b*). In the braid region (see right panel, middle row), the power spectrum shows a peak at $d \sim 5.5$, pointing to crossing of the SCI-induced vortex tubes (see the left bottom panel in figure 3) through the braid. However, there seems to be some activity at smaller wavenumber occurring at the stagnation point at a lower value of d. As shown in figure 6, this is associated with the SPI attempting to emerge on the braid, only for it to run out of time as a consequence of the turbulent collapse of the billow due to the rapid growth of the SCI. This can be clearly seen by virtue of the domination of the total PSD curve by that of the core in the left panel for the $t = 75$ row in figure 7. By $t = t_{3D}$ (bottom panel of figure 7), three-dimensional perturbations have saturated, the flow is turbulent, energy is well distributed over smaller scales, and the flow is well on the way to relaminarization due to continuing dissipation of energy in the absence of external forcing.

As the final stage in our analysis of the low-Reynolds-number cases, we explore the exchange of energy between reservoirs of kinetic and potential energies of the total flow field, and also investigate the sources of energy for 3D perturbations in detail. Figure 8 shows plots of the potential energies (left column) and energetics of the 3D perturbations (right column) for $Re = 750$ and 1000. The potential energy plots can be best interpreted if considered together with the data show on figure 2. These results demonstrate that, as the primary KH billow rolls up, energy is transferred into the potential energy reservoir mostly in the form of available potential energy. During this phase, little mixing occurs and so the background potential energy does not rise significantly. Once the vortex cores grow sufficiently large, however, $\mathscr{P}_B$ rises rapidly due to two factors: first, by extracting energy from the background kinetic energy reservoir through enhanced molecular diffusion inside the vortex cores which is facilitated by a significant increase in the area of the contact surface between light and heavy fluid; second, shortly after t_{2D}, 3D perturbations grow rapidly, extracting their energy primarily from the available potential energy reservoir as is clearly shown by the decrease in the $\mathscr{P}_A$ curve. Growth of 3D perturbations is associated with the diapycnal mixing of light and heavy fluid which contributes to the increase in $\mathscr{P}_B$. A second increase in available potential energy (and, hence, in the total potential energy) is marked by the arrows and corresponds to the turbulent-phase upscale cascade which, as mentioned earlier, occurs at the expense of the kinetic energy of the background shear flow and also leads to a slight reduction in energy transfer into small-scale 3D instabilities.

The rightmost panels of figure 8 illustrate the decomposition of the growth rate of the 3D perturbations (σ_{3D} shown by solid black line) into the various components defined in (2.18). During the early stages of growth of 3D instabilities, σ_{3D} is strongly dominated by the contribution of the buoyancy flux. This is due to dominance of the buoyancy-driven SCI instability inside the cores. Moreover, 3D instabilities extract some energy from the shear associated with the primary KH billow (the $\mathscr{S}h$ term), and from the background flow through the action of the Reynolds stresses (the $\mathscr{R}_{3D}$ term). Some of the energy of the 3D perturbations is lost due to the action of the
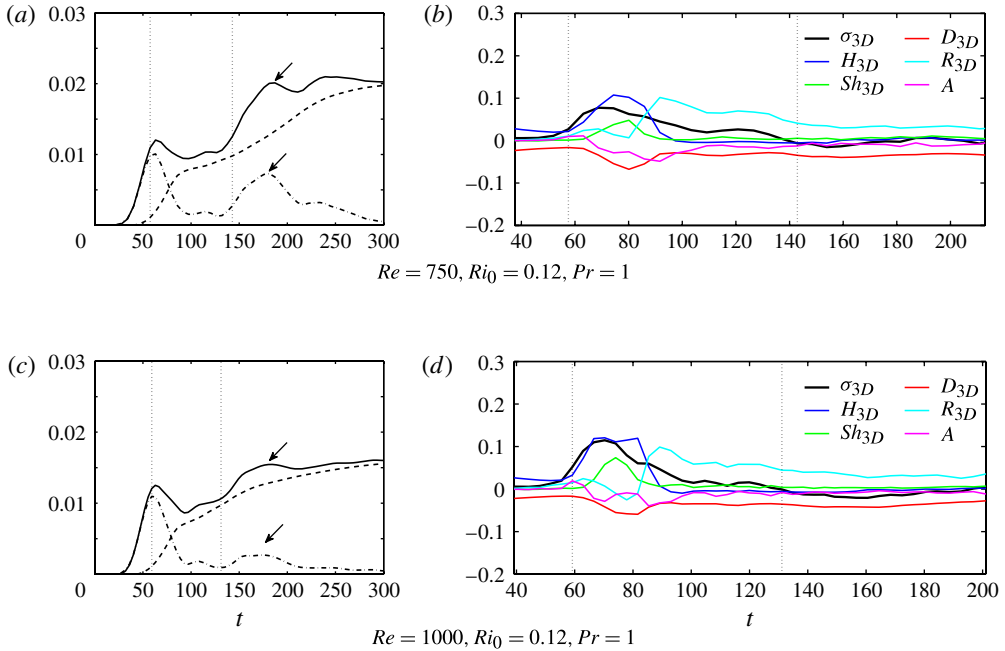
FIGURE 8. (*a,c*) Time variation of calibrated total potential energy ($\mathscr{P}(t) - \mathscr{D}_{\mathscr{P}}t - \mathscr{P}(0)$) in solid line, calibrated available potential energy ($\mathscr{P}_A(t) - \mathscr{P}_A(0)$) in dashed-dotted line and calibrated background potential energy ($\mathscr{P}_B(t) - \mathscr{D}_{\mathscr{P}}t - \mathscr{P}_B(0)$) in dashed line. (*b,d*) Time variation of various terms of (2.18). The vertical dashed lines in the right panel represent t_{2D} and t_{3D}. Time period beyond t_{3D} can be considered as most relevant to the Osborn formula given in (1.1).

stretching deformation (the $\mathscr{A}$ term) because of the existing anisotropy in the flow field. Figure 8 shows that by the time t_{3D}, the contributors to σ_{3D} have decayed significantly, leaving a balance between energy extraction from the background shear by means of Reynolds stresses, the energy loss through viscous dissipation, the turbulent buoyancy flux and the anisotropy term, with the latter two contributions being much less than the former two. This balance is maintained throughout the turbulent phase of the flow. Had the anisotropy term decayed to zero in the turbulent phase of the flow, the balance between shear production, dissipation and buoyancy flux would be exactly that assumed in derivation of the Osborn formula given by (1.1), and the ratio of buoyancy flux to the production term would be the flux Richardson number. However, the fact that the turbulent phase anisotropy term is of the same order as the buoyancy flux term (as can be seen in the figure) indicates that the use of (1.1) to infer an effective diffusivity would involve some error due to the neglect of the anisotropy. This error will be quantified in subsequent sections. It is also important to note that prior to t_{3D}, a considerable amount of mixing occurs which is due to enhanced diffusion facilitated by the roll-up of the KH vortex cores. This portion of the vertical flux is often missed in the inference of vertical diffusivity values from observational data, as a consequence of two contributing factors: first, common correlations which relate the measured dissipation to flux (such as (1.1)) only consider the fully turbulent phase of the flow, and second, preturbulent roll-up of KH waves can go undetected by microstructure measurement techniques.
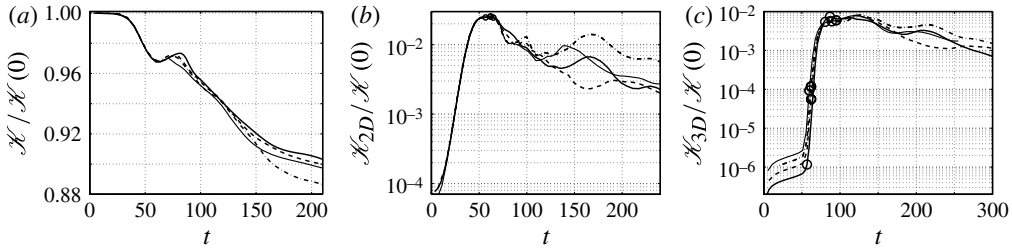
FIGURE 9. Same as figure 2 for $Re = 4000$ (thick solid lines), $Re = 6000$ (dashed line), $Re = 8000$ (dashed-dotted line) and $Re = 10\,000$ (thin solid line).

3.2. *The high-Reynolds-number regime*

We next turn our attention to cases with higher Reynolds numbers. Specifically, we shall explicitly consider the variations of the results for the values $Re = 4000$, 6000, 8000 and $10\,000$ all at $Ri_0 = 0.12$ and $Pr = 1$. Figure 9 illustrates the evolution of the various compartments of kinetic energy for the four cases. In general, the graphics are organized in the same way as those in figure 2: increase in $\mathcal{K}_{2D}$ (at the expense of the kinetic energy of the background flow) due to growth of the primary KH wave, followed by rapid growth in $\mathcal{K}_{3D}$ facilitating transition to turbulence. Certain important differences exist, however, between the higher Re cases of figure 9 and those of figure 2. At lower Re, three-dimensional perturbations begin to grow shortly after saturation of the primary KH billow, whereas at higher Re, they initiate earlier during the roll-up of the KH billow (noting that the first circle on lines in figure 9(c) represents t_{2D}). This implies that 3D instabilities can modify the primary KH wave on a global or local scale (depending on the type of growing 3D modes) at early stages of its evolution. This is consistent with predictions of Mashayek & Peltier (2012b) which showed that increase in Re leads to increase in growth rate of most of the unstable secondary instabilities and also leads to the possibility of earlier emergence of secondary modes during flow evolution. As will be described later, this might have important implications for the interpretation of observations of shear instabilities in geophysical flows. Two additional points can be made by comparing figures 2 and 9: first, although at lower Re the growth rate of $\mathcal{K}_{3D}$ increases with Re, it seems that once Re is sufficiently high this growth rate saturates, and $\mathcal{K}_{3D}$ grows to its maximum from a negligible value in a very short period of time; second, the second peak in $\mathcal{K}_{2D}$, which is associated with a turbulent-phase upscale cascade (an apparently weak form of vortex pairing), becomes less significant with the increase in Re. This is because the increase in Re promotes earlier and faster growth of a number of 3D modes (the number of which itself increases with Re; see Mashayek & Peltier (2012a)) and thereby, efficiently destroys the large-scale coherent structure of the KH wave which is necessary for accommodation of the pairing instability. The dependence of the degree of suppression of the pairing instability with increase in Re will be examined in detail in the next section.

Figure 10 shows plots of streamwise and spanwise vorticity isosurfaces at various times between t_{2D} and t_{3D} for each of the cases we are considering. Figure 11 shows the corresponding plots of PSD, as well as contour plots of vorticity on planes passing through the braid and core regions. In what follows, we will interpret these two figures together to discuss the differences in the evolution of the flow for each Reynolds number.
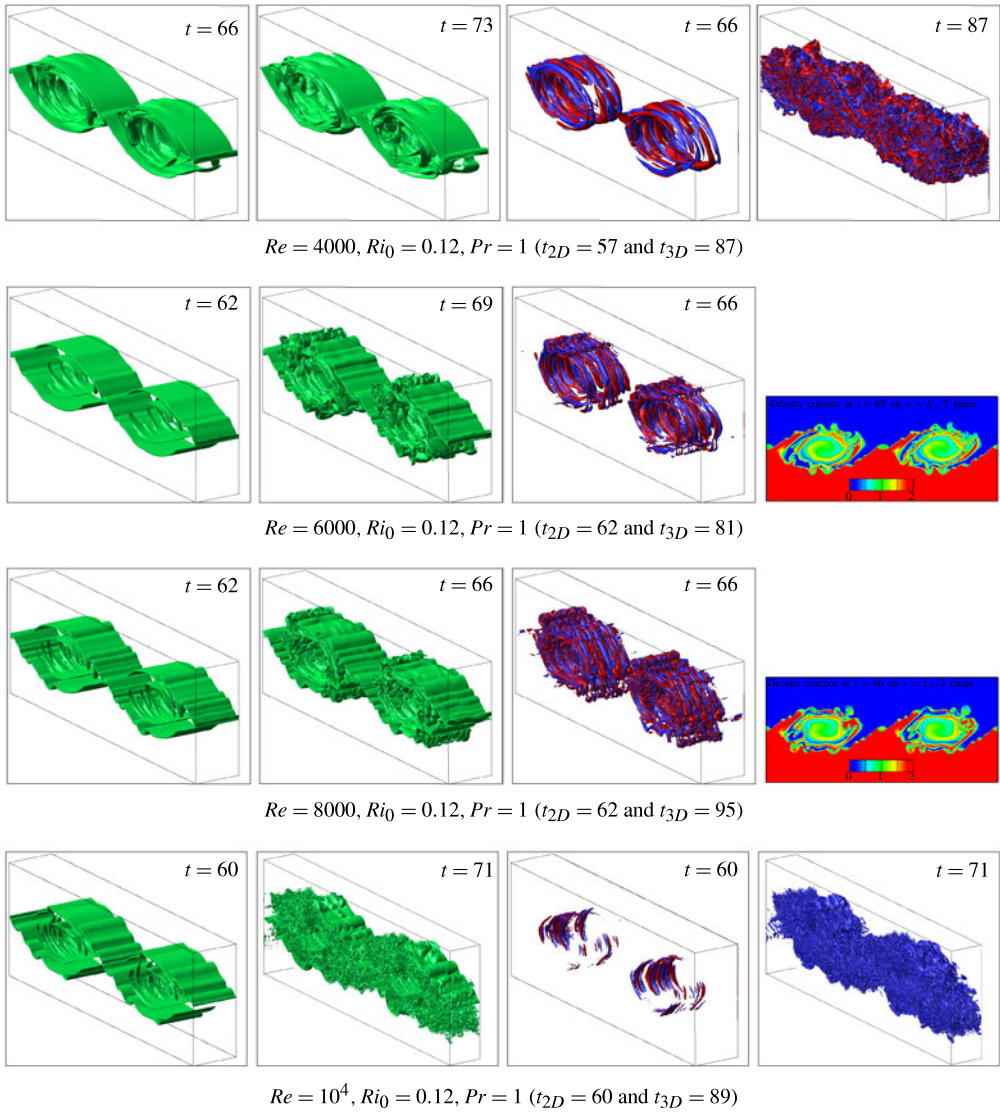
FIGURE 10. Same as figure 3 but for $Re = 4000$, 6000, 8000 and 10 000. Density contours are shown for the $y = L_y/2$ planes for $Re = 6000$ and 8000 cases. In the last panel of the bottom row, only blue isosurfaces are shown for better visual presentation of the streamwise vorticity, ω_x.

For $Re = 4000$, two 3D modes begin to grow shortly after t_{2D}. SCI grows in the cores while a stationary (with respect to the primary KH billow) vortex forms at the stagnation point on the braid due to emergence of SPI. Inspection of the PSD for this case shows that the two modes (SCI and SPI) have different spanwise wavenumbers, with that of the SCI being larger. Moreover, as one would expect, most of the power in the spectrum for the total flow field is concentrated in the modes associated with the core region. The middle and right panels in the first row of figure 11 show growth of convectively unstable rolls in the vorticity layers inside the cores, as well as the SPI
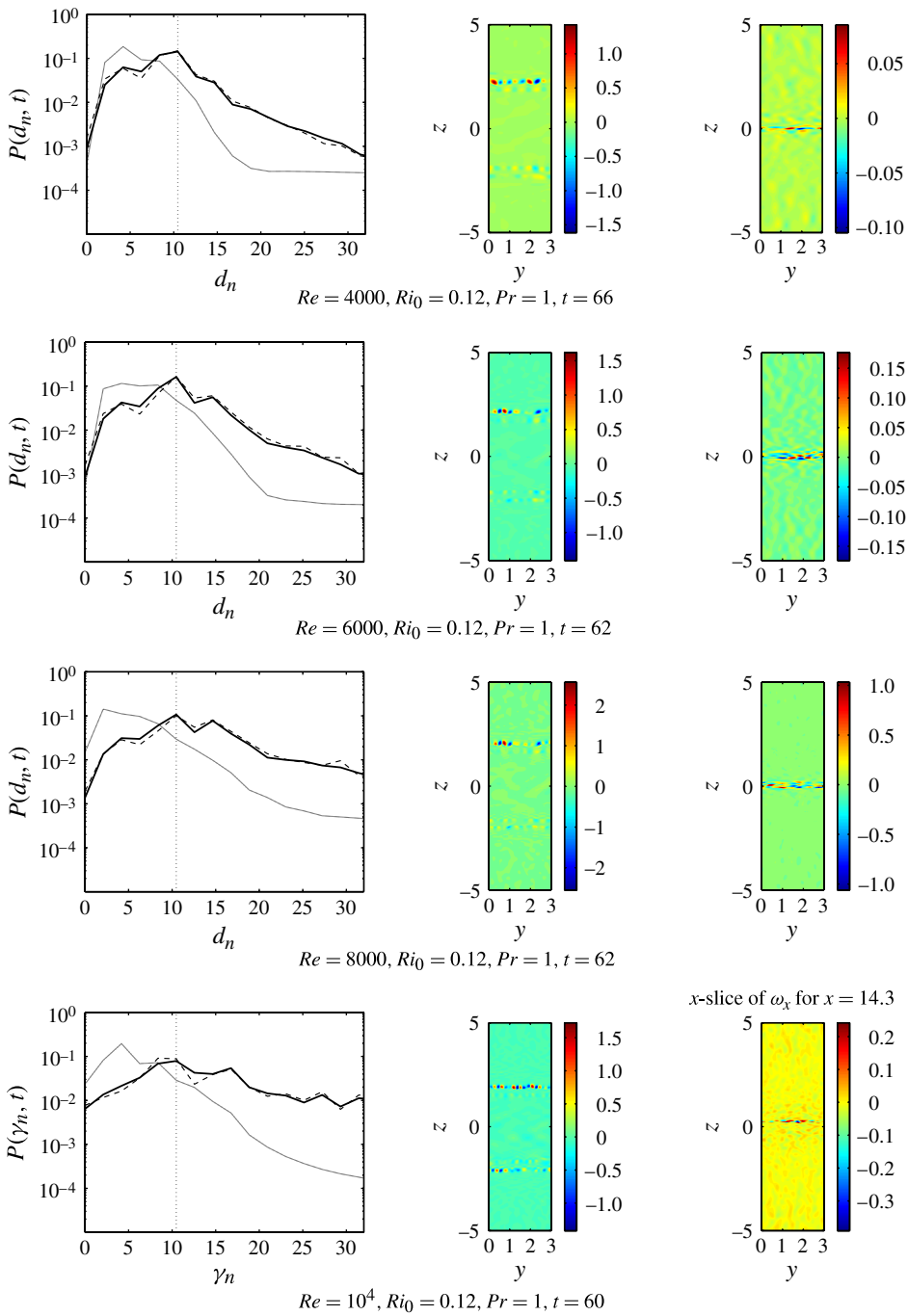
FIGURE 11. Same as figure 7 for $Re = 4000$, 6000, 8000 and $10\,000$. Times of plots for each Reynolds numbers is chosen to be within the period of rapid rise in $\mathcal{K}_{3D}$ shown in figure 9(c).

vortex (with a different wavenumber) forming at the braid stagnation point. The core curve in the PSD plot has a secondary peak (at $d \sim 5$) which is the same wavenumber as that of the SPI vortex on the braid. This is not coincidental: as discussed in Mashayek & Peltier (2012*a*), because the SPI can interact with the largest vorticity bands inside the cores (which host the LCVI; see figure 23 in appendix A). The interaction between the two gives rise to a non-local mode which Mashayek & Peltier (2012*a*) refer to as SVBI (see appendix A), which leads to formation of a SPI vortex on the braid as well as deformation of the vorticity bands inside the cores which have approached the stagnation point due to growth of the vortex cores. This further confirms the prediction of Mashayek & Peltier 2012*b* that SVBI is a combination of SPI and LCVI (or, alternatively, one might consider SPI and LCVI as manifestations of SVBI).

Once Re is increased to $Re = 6000$, SSI of the braid joins the group of 3D instabilities already observed at $Re = 4000$. As shown in the right-most panel in the second row of figure 10 (which shows ω_y on a slice passing through the middle of the domain), SPI will be seen to look just like an SSI vortex from this perspective. However, it should be noted that the two instabilities are of different origins (SSI is shear-induced while SPI extracts its energy from the background strain field), and these modes have different wavenumbers (SSI is nearly 2D while SPI is 3D as shown in the left and right panels of figure 11). The SSI vortices propagate on the braid towards the vortex cores while the SPI-induced vortex is locked on the stagnation point. The propagation of SSI vortices towards the cores has significant implications for the collapse of the vortex cores into fully developed turbulence. As shown in figure 10, SSI vortices distort the outer layers of the cores, exciting various tertiary instabilities such as Rayleigh–Taylor instability (see the right panels in rows two and three of figure 10 and Mashayek & Peltier (2012*b*) for further details). This enhancement in the breakdown of the cores due to SSI vortices can precede or coexist with the destructive influence of the SCI.

A comparison between $Re = 6000$ and 8000 cases in figure 10 reveals a great similarity between the two cases, with the scales of structures produced by secondary and tertiary instabilities becoming smaller with Re. Moreover, the number of SSI vortices increases, and the time of onset of their emergence shifts to earlier times with increase in Re. Once Re is increased to $10\,000$, SSI vortices dominate the braid early on in the evolution of the KH billow and during the roll-up of the cores, and thereby prevent the SPI vortex from emerging at the stagnation point. Therefore, it seems that at the assumed values of Ri_0 and Pr, SPI can exist only over an intermediate range of Reynolds number.

The general conclusions based upon the information provided in the graphics of figures 3 and 10 is that within the range of $750 < Re < 10\,000$ (for $Ri_0 = 0.12$ and $Pr = 1$), numerous secondary instabilities are expected to and do emerge. At low Re, the pairing instability continues to be a key player which enforces a strong upscale cascade, while its occurrence seems to be increasingly modified by the emergence of a group of small-scale instabilities growing in the cores or on the braid as Re is increased. These secondary instabilities may coexist or may interfere with or even prevent the emergence of each other depending on the order of their appearance (which itself is highly sensitive to the background noise in the flow field). The differences in the underlying dynamics of the turbulent collapse of the mixing layer due to the emergence of different instabilities can have important implications for turbulent properties of the flow such as the efficiency of mixing. We will explore this in the next section.
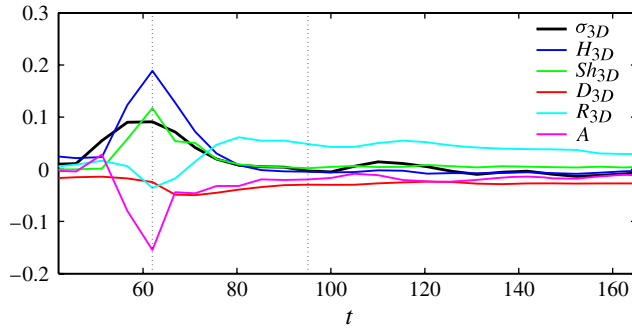
FIGURE 12. Same as the right panels in figure 8 but for $Re = 8000$.

It is also interesting to note that all of the secondary instabilities found in the non-separable linear stability analyses reported in Mashayek & Peltier (2012*a*,*b*) can be observed in our DNS results. Although some are only observed at Re much higher than that of the stability analyses (which were performed at $Re = 1000$ and 2000), their potential to grow existed even at these lower values of Re. Therefore, further repetition of the non-separable secondary stability analyses at higher Re (say 10 000 for example) might be useful in predicting the occurrence of even further instabilities which might exist at even higher Re values.

A comparison of the various Re cases in figure 11 shows that with increase in Re, more and more energy is pumped into small-scale instabilities emerging inside the vortex cores, while the braid remains dominated by distinct wavenumbers associated with the SPI and SSI modes. For $Re = 10\,000$, there is considerable activity at spanwise wavenumbers above $d = 10$. This is due to the emergence of new instabilities at higher Re in the cores (such as LCVI and shear instability of vorticity layers inside the cores, see Mashayek & Peltier (2012*a*,*b*)), and distortion of the vortex cores due to braid activities (such as the travelling of SSI vortices along the braid and towards the cores which can excite local Rayleigh–Taylor instability in the outer regions of the vortex cores). This enhancement of the growth of various 3D perturbations inside the cores with increase in Re can lead to rapid homogenization of the vortex cores as compared to the evolution of the braid. As shown in the second panel in the last row of figure 10, at $Re = 10\,000$, the cores are completely turbulent while a clear braid layer (with overlying SSI vortices) can still be observed. This might have implications for the interpretation of observations of shear layers, such as those of Geyer *et al.* (2010). Since back-scatter measurements are sensitive to density differences, a side view (obtained from measurements) of a KH billow such as that of figure 10 for $Re = 10\,000$ might overemphasize the importance of braid structures simply because cores have homogenized earlier and faster than the braid regions. This could provide a simple explanation for the existence of almost no structures inside the cores of the KH wave trains reported by Geyer *et al.* (2010).

To compare the energetics of 3D perturbations between high- and low-Re cases, figure 12 shows a plot similar to those shown in figure 8 but for $Re = 8000$. Comparing this plot with those in figure 8 shows that with increase in Re, the contribution of $\mathcal{H}_{3D}$ to σ_{3D} increases due to vigorous overturning of convectively unstable regions inside the vortex cores. There is also a slight increase in the transfer of energy from the background KH billow to the 3D perturbation field (the $\mathcal{S}h$ term). However, these two increases are compensated by the increase in negative

influence (draining of $\mathcal{K}_{3D}$) due to enhanced dissipation ($\mathcal{D}$) and anisotropy in the field ($\mathcal{A}$). The latter is due to increase in emergence of various secondary modes of different origins (buoyancy-driven, shear-induced, strain-induced, etc.) and with different wavenumbers. The figure also reveals a small negative influence (i.e. transfer of energy from the 3D field to the background flow) of Reynolds stresses ($\mathcal{R}_{3D}$) during very early periods of growth of 3D perturbations. Similar to low-*Re* cases, in the turbulent phase of the flow ($t > t_{3D}$), there is a dominant balance between $\mathcal{R}_{3D}$, $\mathcal{D}_{3D}$, $\mathcal{H}_{3D}$ and the anisotropy term ($\mathcal{A}$), with the latter playing a more important role at high *Re*. Therefore, the non-zero contribution of anisotropy breaks down the three-way balance of $\mathcal{R}_{3D}$–$\mathcal{H}_{3D}$–$\mathcal{D}_{3D}$ which underlies (1.1). With inclusion of $\mathcal{A}$ in the balance, the turbulent phase mixing efficiency, which can be calculated from

$$\mathcal{E}^{3D} = \frac{\mathcal{M}}{\mathcal{M} + \mathcal{D}_{3D}} \approx \frac{\mathcal{H}_{3D}}{\mathcal{H}_{3D} + \mathcal{D}_{3D}} = \frac{\mathcal{H}_{3D}}{\mathcal{R}_{3D} - \mathcal{A}}, \tag{3.1}$$

is clearly larger than the flux Richardson number $R_f = \mathcal{H}_{3D}/\mathcal{R}_{3D}$ due to non-zero anisotropy. This is one of the reasons why the time-averaged turbulent mixing efficiencies which we will present in the following section will be higher than the canonical value of 0.2 that has been assumed in inferring the diapycnal turbulent diffusivity on the basis of ocean microstructure measurements.

4. Route to turbulence, mixing efficiency and effective diffusivity

In this section, we quantify the extent to which emergence of 3D instabilities at higher Reynolds numbers suppress the pairing process. We also investigate how this suppression, as well as the increase in the number and growth rate of 3D secondary modes with *Re* change the route to mixing and thereby affect the efficiency of mixing and the effective vertical flux. This will assist in providing a sound answer to the question posed in the title of this article.

Figure 13 shows plots of time evolution of PSD of the primary KH wave (in figure 13*a*) and the pairing mode (in figure 13*b*) for various Reynolds numbers, all at $Ri_0 = 0.12$. The primary instability curves follow more or less the same pattern during the roll-up of the KH wave since growth rate of the KH wave is primarily a function of stratification. However, the pairing mode curves show that there is a highly significant reduction in the transfer of energy into the pairing instability with increase in *Re*. Consistent with the flow visualization plots shown in the previous section, at $Re = 750$, pairing is the only secondary mode growing on the primary KH wave other than the SCI. From $Re = 750$ to $Re = 1000$, however, earlier and faster emergence of SCI as well as emergence of stagnation point instabilities (see figures 3, 4 and 6 and their corresponding discussions) lead to noticeable suppression in PSD$_{pairing}$. The level of suppression remains nearly the same from $Re = 1000$ to $Re = 4000$, beyond which emergence of a number of other modes (such as the SSI, LCVI and other instabilities they excite inside the vortex cores) results in a further suppression of the subharmonic mode. This second stage of sharp suppression in PSD$_{pairing}$ is consistent with observations of figure 10. Although suppression of vortex pairing by stratification has been long known, figure 13(*b*) provides clear evidence of the suppression of pairing by an increase with *Re* of the number and growth rate of small scale structures. This agrees with the paucity of observational evidence for vortex mergers in shear layers at geophysically relevant high Reynolds numbers.

Figure 13(*c*) plots the time evolution of instantaneous mixing efficiency for the four cases considered in figure 13(*a*,*b*). As discussed in Mashayek & Peltier (2012*b*),
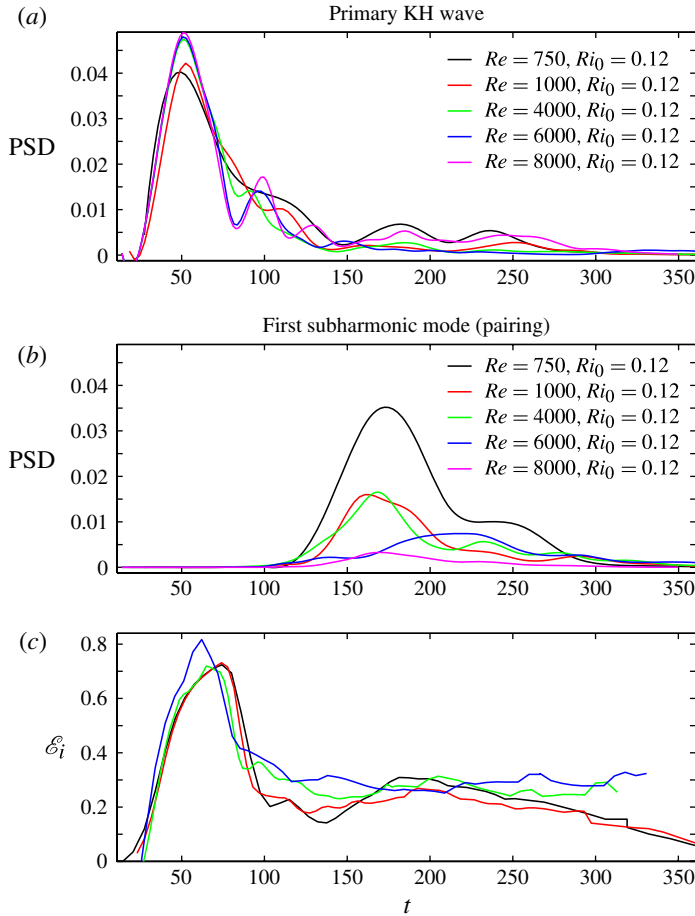
FIGURE 13. PSD for the primary KH wave (*a*) and the first subharmonic wave (*b*) for various Reynolds number all at $Ri_0 = 0.12$; the corresponding instantaneous mixing efficiency in (*c*).

the preturbulent phase of a shear layer lifecycle can be highly efficient in the vertical mixing of dense and light fluid mostly due to the small dissipation rate which is characteristic of this stage of flow evolution. During the transition and post-transition phases of the flows (i.e. $t > t_{2D}$) mixing can however be greatly influenced by the details of the underlying dynamics. As mentioned earlier in discussion of flow energetics, for $Re = 750$, the turbulent-phase pairing extracts some of its energy from the $\mathscr{K}_{3D}$ reservoir. This leads to a decrease in the effective viscous dissipation facilitated by small-scale perturbations and thereby leads to an increase in $\mathscr{E}_i$. With increase in Re and suppression of pairing, the 3D perturbation field becomes more energetic and this increases the viscous dissipation. However, an energized 3D perturbation field also enhances diapycnal mixing considerably. The interplay between these opposing factors (in the sense that one tends to increase and one to decrease $\mathscr{E}$) leads to a decrease in the turbulent-phase-averaged $\mathscr{E}$ from $Re = 750$ to $Re = 1000$ (due to suppression of pairing) and an increase in turbulent-phase-averaged $\mathscr{E}$ from $Re = 1000$ to $Re = 4000$ (due to increase in diapycnal mixing $\mathscr{M}$). From $Re = 4000$ to higher Reynolds number $\mathscr{E}_i$ seems to be only mildly influenced by the increase
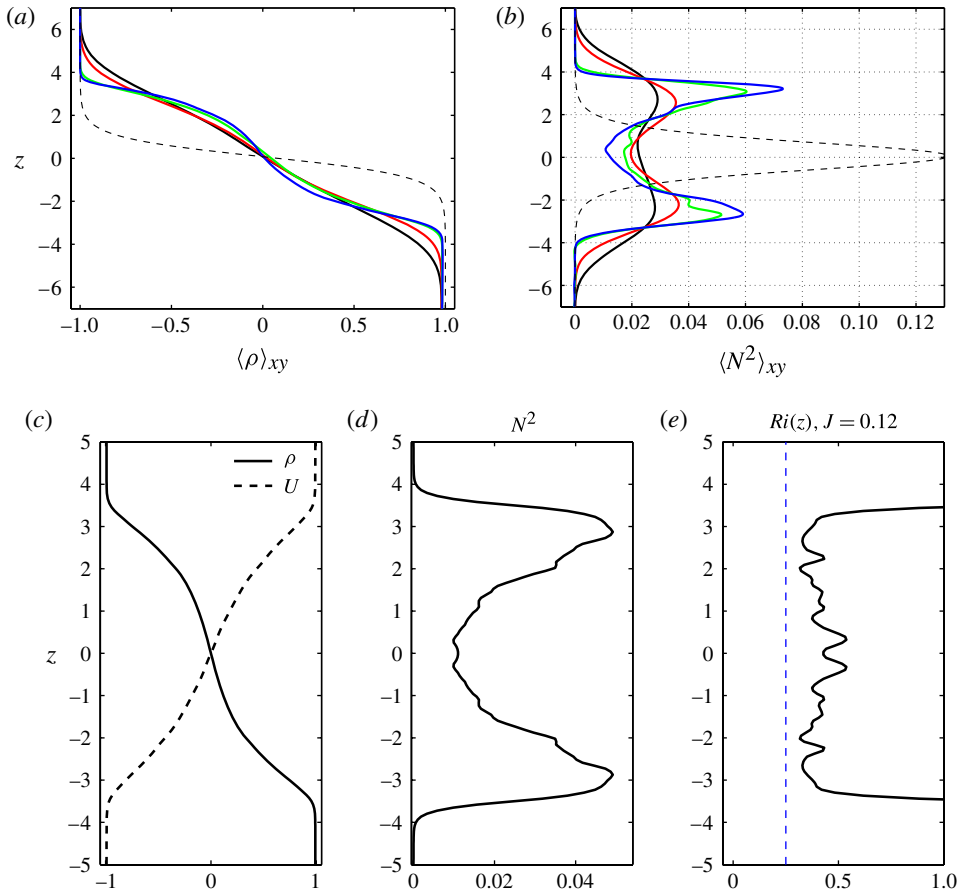
FIGURE 14. Spatially averaged density field after relaminarization of the layer (in (*d*)) and spatially-averaged buoyancy frequency after relaminarization of the layer (in (*e*)) for the same cases as shown in figure 13. Line colour attributes in (*a,b*) are the same as figure 13 with the thin dashed black curves representing the profiles associated with the initial shear layer prior to roll up of the primary KH wave. The lower row shows the relaminarized-state profiles for the $Re = 6000$ case, with the left frame showing the density and velocity profiles, the middle frame showing the buoyancy frequency squared, and the right frame showing the gradient Richardson number.

in number and decrease in scales of 3D secondary modes. Figure 13(*b*) illustrates the clear and considerable change in efficiency of mixing with the change in the dynamical processes responsible for turbulence breakdown of the shear layer.

In addition to the influence of vortex merging on mixing properties, this process also influences the effective entrainment of the high- and low-density fluids located beneath and above the layer. This is because vortex pairing at small Reynolds number is associated with significant vertical displacement of the vortex cores and this results in 'thickening' of the mixed layer. However, with increase in Re and subsequent suppression of pairing, the effective 'thickness' is expected to decrease. This is shown in figure 14(*a*) which shows spatially averaged profiles of the density field at late stages in the lifecycle of the shear layers in which $\mathcal{K}_{3D}$ has decayed and the flow has relaminarized. For $Re = 6000$, the final layer thickness is approximately 50 %

less than the thickness for the $Re = 750$ case. Moreover, the layer seems to be more well-mixed at lower Re while an intermediate step forms in the middle of the layer for high-Re cases. This is better demonstrated in figure 14(b) of the figure which plots the N^2 profiles for the same cases. The strong double peak associated with $Re = 6000$ becomes even larger and sharper for $Re = 8000$ and $10\,000$ (not shown here) which suggest that the resulting density profile would most probably be susceptible to a new cycle of primary and secondary shear instabilities if a sufficiently sheared mean flow were to be imposed. The bottom row in figure 14 shows volume-averaged profiles of density, streamwise velocity, buoyancy frequency squared and gradient Richardson number for the relaminarized flow of the case for $Re = 6000$. The left frame shows that the resulting velocity profile is also layered. This profile, however, is subject to change as the shear forcing changes due to time evolution of the background flow. The right panel shows that $Ri_0 > 0.25$ at all depths, meaning that the laminarized flow is stable to shear instabilities, and therefore new forcing is required to enable a second lifecycle of shear instability. It is well-known that the final state of a KH billow leads to bulk Richardson numbers of greater than 0.25 (see Smyth & Moum 2000 for a discussion). The stability of the laminarized density profiles (figure 14a) depends on the nature of the shear imposed on them which itself depends on the nature of the shear layer environment. For example, for shear-induced wave trains growing at the peaks of low-frequency internal-tide-induced internal waves in the deep ocean, one can imagine the existence of a continuous but modulating shear forcing induced by the tides. Further investigation of the stability properties of profiles such as that in figure 14(e) is not the focus of the present work but it is interesting to point out that formation of a three-layer density structure from an initially two-layer profile after one cycle of shear instability opens the door for primary shear instabilities specific to multilayer systems (Caulfield 1994; Lee & Caulfield 2001).

From a practical perspective, perhaps the most important quantity related to a shear layer is the vertical flux of tracers across the layer. This vertical flux is often parameterized through the introduction of subgrid-scale mixing representations in ocean general circulation models (OGCMs). To investigate the influence of specific transition scenarios (associated with the dominance of various secondary instabilities on the transition process) on the vertical flux, we plot the total and perturbation vertical buoyancy flux for the four cases considered previously (in figure 13) in figure 15. During the period $t < t_{2D}$, total flux is dominated by that associated with the roll-up of the primary KH wave and consists of a large upward flux followed by a smaller downward net flux. At low Re, vortex pairing also contributes significantly to the upward flux. With increase in Re and suppression of pairing however, the post transition total buoyancy flux (for $t > t_{3D}$) becomes dominated by the flux associated with the small-scale turbulent motions. It is also important to note the decrease in the $t_{2D} - t_{3D}$ gap with increase in Re. As shown for $Re = 8000$ and $10\,000$ in the previous section, for sufficiently high Re, $\mathcal{K}_{3D}$ begins to grow prior to t_{2D} and leads to rapid collapse of the layer and complete suppression of an upscale cascade of energy. However, the net upward flux associated with the roll-up of the primary shear mode is significantly larger in magnitude than the turbulent phase buoyancy flux, although it occurs over a short period of time. We will shortly assess the error introduced by exclusion of this portion of vertical flux in the calculation of the total flux at geophysically plausible Reynolds numbers.

To examine the applicability of relation (1.1) to the problem of predicting the effective diffusivity of shear-induced turbulence, we apply it in the analysis of the results of our numerical simulations of turbulent shear-layer collapse. Figure 16 shows
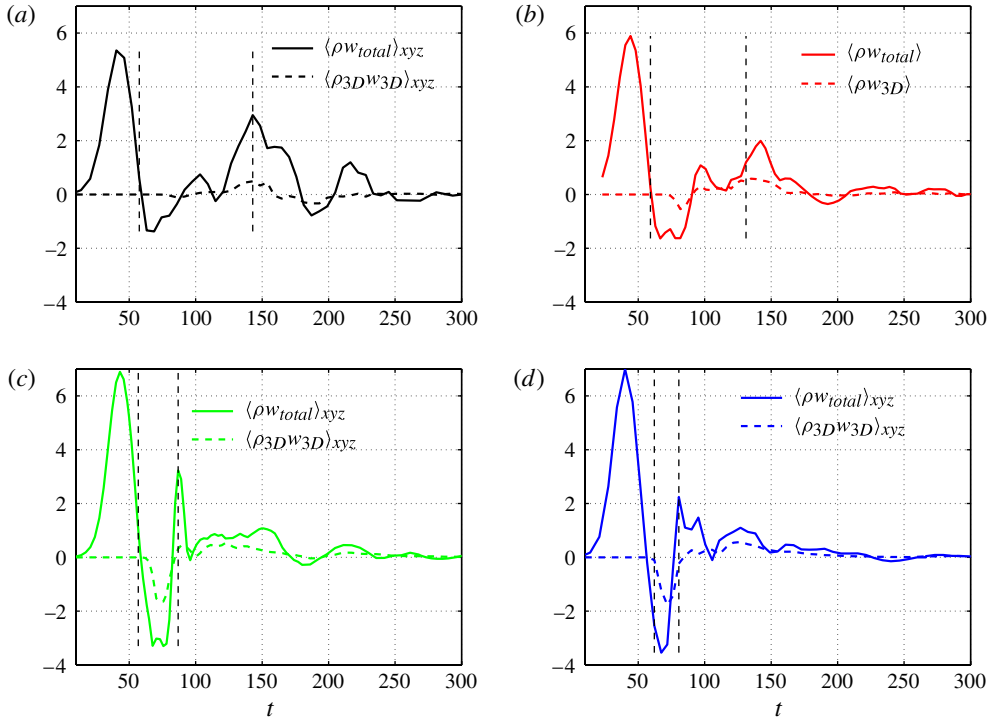
FIGURE 15. (Colour online) Time evolution of total and perturbation buoyancy fluxes for the four cases considered in figure 13: (*a*) $Re = 750$, $Ri_0 = 0.12$; (*b*) $Re = 1000$, $Ri_0 = 0.12$; (*c*) $Re = 4000$, $Ri_0 = 0.12$; (*d*) $Re = 6000$, $Ri_0 = 0.12$. Colour coding is also the same as figure 13. The two dashed lines in each panel represent t_{2D} and t_{3D}.

plots of κ calculated using (1.1). Two sets of calculations are performed based on this formula: in one we keep mixing efficiency constant at the commonly used value of 0.15 and in the second we use the actual time series of mixing efficiency calculated for each case based on the simulation results. The two calculations are tested against an accurately defined effective diffusivity calculated on the basis of buoyancy fluxes which were plotted in figure 15 and by using the following relation

$$\langle \rho w \rangle = \kappa \frac{d\bar{\rho}}{dz}, \qquad (4.1)$$

where $\bar{\rho}$ is the background density.

Left panels of figure 16 show the three calculated diffusivity profiles while the right panel in each row shows a close-up of the turbulent phase ($t \Rightarrow t_{3D}$) of the curves. At all Reynolds numbers, there are significant differences between the black curves and the Osborn-relation-based predictions for an entirely expected reason: namely that relation (1.1) is based upon the assumption of statistically steady turbulent flow and is therefore not expected to be applicable for the pretransition phase of flow evolution. The early period of strict inapplicability of (1.1) is much more extended at lower Reynolds numbers as t_{3D} is inversely related to Re. Moreover, a prominent presence of pairing instability at low Re hinders the transition to semi-isotropic stationary turbulence by both breaking the isotropy assumption and by extracting energy out of the 3D perturbation kinetic energy reservoir. With increase in Re, however, the
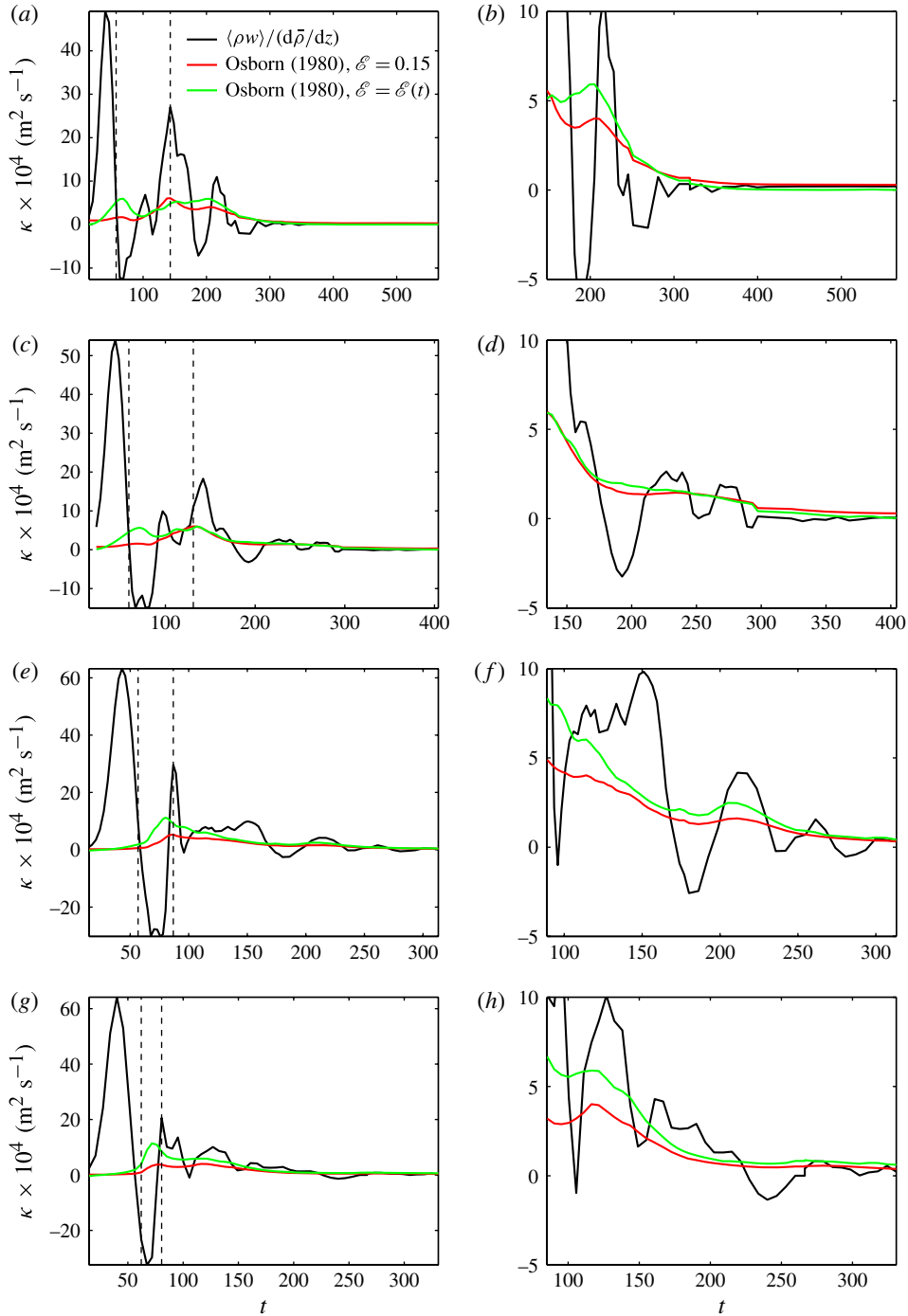
FIGURE 16. Effective diffusivity calculated by using (4.1) in black lines, and by using Osborn relation (1.1) with $\mathscr{E} = 0.2$ in red lines and with considering the actual time history of $\mathscr{E}$ in green lines. Each row corresponds to one of the cases discussed in figures 13 and 15. The right panel in each row is a close-up of the turbulent phase (i.e. $t > t_{3D}$) of the left panel: (*a,b*) $Re = 750$, $Ri_0 = 0.12$; (*c,d*) $Re = 1000$, $Ri_0 = 0.12$; (*e,f*) $Re = 4000$, $Ri_0 = 0.12$; (*g,h*) $Re = 6000$, $Ri_0 = 0.12$.

difference between the predictions of (1.1) and the accurate flux becomes more limited to the early roll-up stage of the shear instability. However, this difference remains an important contributor to the error in total flux that one would make by using (1.1). The expanded resolution versions of the turbulent phase of the diffusivity curves (in the right panels) show that well into the turbulent phase of flow evolution, relation (1.1) gives a good estimate of the effective diffusivity. Most observational evidence obtained in support of κ has been limited to turbulent flows since preturbulent large-scale motions prior to transition to turbulence are not meant to be measured by microstructure measurement techniques. However, figure 16 shows that a large vertical flux is associated with less turbulent, more coherent large structures which develop prior to transition to turbulence. Therefore, insofar as the vertical flux is concerned, there is an error associated with the early stages of flow evolution which includes the roll-up process and vortex pairing. As discussed earlier however, with increase in Re, pairing is suppressed and the roll-up process becomes shorter and the fully developed turbulent contribution to the total flux is therefore expected to dominate the total flux.

To quantify the errors in a time-averaged sense, we plot time-averaged cumulative mixing efficiency versus Reynolds number in figure 17(*a*). Two curves are plotted one for $\mathscr{E}_c$ integrated over the whole lifecycle of shear-layer evolution and one only integrated over the turbulent phase of the flow. The result shows that only the post-transition integrated efficiency at low Reynolds numbers is in the conventional range of 0.15–0.2 (as was illustrated in Caulfield & Peltier (2000)). However, with increase in Re, $\mathscr{E}_c^{post3D}$ initially decreases (due to suppression of pairing) and then increases (due to more efficient diapycnal mixing energized by the emergence of a large number of 3D instabilities) leading to values in excess of 0.3. Therefore, even if the preturbulent phase of the flow becomes short and negligible at very high Reynolds number (an assumption which we have not attempted to address directly in this paper), $\mathscr{E} = 0.15$–0.2 seems to be low for shear-induced mixing.

Figure 17(*b*) shows a plot similar to figure 17(*a*) but for the total viscous dissipation. At low Reynolds numbers, time-averaged dissipation is dominated by KH roll-up and the pairing process due to lack of emergence of 3D instabilities during later times of flow evolution. Increase in Re, however, leads to partial suppression of pairing (and its associated enhanced dissipation) and emergence of the SPI. Rapid introduction of spanwise small-scale structures associated with the SPI leads to the post-transition dissipation dominating the lifecycle-averaged dissipation. Further increase in Re leads to significant suppression of pairing and emergence of other small-scale instabilities (such as the SSI, LCVI etc.). In this high-Re regime (beyond $Re = 6000$), the preturbulent phase of flow evolution is much shorter than the turbulent phase, and $\mathscr{D}$ is completely dominated by turbulent phase contributions.

Figure 17(*c*) shows time-averaged (over the whole lifecycle of unstable shear layer evolution) values of κ for the profiles shown in figure 16. The differences between the curves in this figure illustrate the errors introduced into estimates of the vertical buoyancy flux due to different contributors discussed above: the difference between the solid black curve and the dashed black curve is entirely due to ignoring the preturbulent flux. This large contribution does not seem to become negligible within the Reynolds number range explored in this paper, suggesting that even though the preturbulent phase of flow evolution becomes shorter with increase in Re, its contribution to total buoyancy flux remains important. The difference between the dashed black curve and the red curve, both of which correspond to the fully developed turbulent phase of the flow, is only due to the error associated with the isotropy assumption that underpins relation (1.1) since a time-variable mixing efficiency is
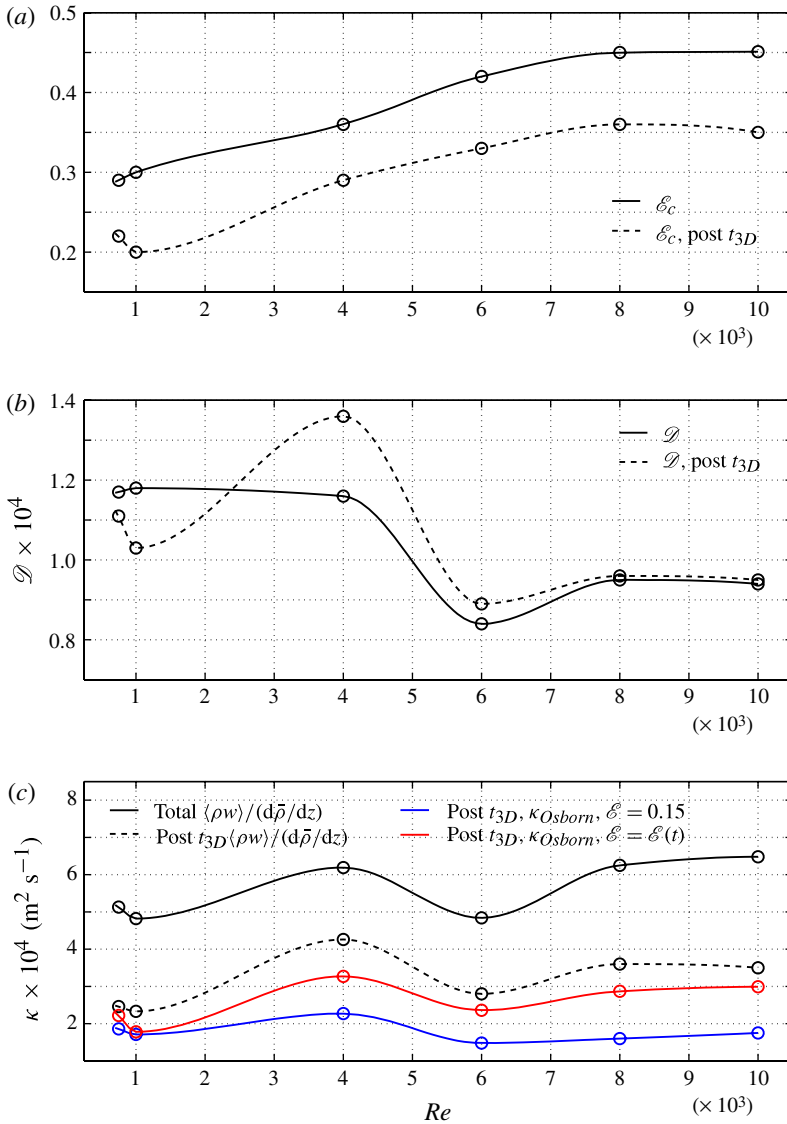
FIGURE 17. (*a*) Cumulative mixing efficiency (spanning both pre- and post-turbulent phases of the flow) shown as a solid black line and post-transition cumulative efficiency (only spanning the turbulent phase of the flow) shown as a dashed black line as a function of the Reynolds number. (*b*) Total dissipation $\mathscr{D}$ averaged over both pre- and post-turbulent phases in solid black and $\mathscr{D}$ averaged only over the fully developed turbulent phase in dashed black line. (*c*) Plotted against the Reynolds number are: the time-averaged (over the lifecycle of the shear layer) effective diffusivity calculated by using (4.1) in black, post-t_{3D} time-averaged effective diffusivity calculated from (4.1) in dashed black line, effective diffusivity calculated from Osborn's relation (1.1) with time-dependent $\mathscr{E}$ in red and Osborn's relation with $\mathscr{E} = 0.15$ in blue.

employed in (1.1) to obtain the red curve. The time history of mixing efficiency is often not known in practical applications of relation (1.1). Therefore, the difference between the dashed black line and the blue line (which is obtained by using

Re	750	1000	2000	4000	6000	8000	10 000
Re_b	82	108	188	383	433	502	610

TABLE 2. Turbulent phase buoyancy Reynolds numbers.

relation (1.1) along with the often used mixing efficiency value of $\mathscr{E} = 0.15$) should be considered as a practical measure of the error associated with employing relation (1.1) with the canonical value of 0.2 for $\mathscr{E}/(1 - \mathscr{E})$ (or 0.15 for $\mathscr{E}$) to a fully developed shear-induced turbulent layer. This error, which amounts to an under-prediction of the flux by almost 100 %, is primarily due to the low constant value used for $\mathscr{E}$. According to figure 16(a), a value of $\mathscr{E} \sim 1/3$ would lead to better predictions for our cases. It is important to note that the relatively large variations in diffusivity curves in figure 16(c) follow the variation of the dissipation curves in figure 16(b) which was explained in terms of the emergence of different modes of instability at various Reynolds numbers. The mixing efficiency in figure 16(a) seems to be less variable at sufficiently large Reynolds numbers. It is also important to note that the agreement between the actual effective diffusion and that obtained by using the Osborn formula along with $\mathscr{E} = 0.15$ is good in the low-Reynolds-number regime, but that it deteriorates with increase in Re. Therefore, our results suggest that emergence of a large number of secondary instabilities, along with suppression of the pairing instability at high Reynolds numbers, lead to deviation of the turbulent phase energy balance upon which the Osborn formula is based.

At this stage, we can assess the extent to which the turbulent mixing represented by the numerical experiments described in this study might be of relevance to shear-induced mixing in the oceans. A relevant parameter for this purpose is the buoyancy Reynolds number defined as $Re_b = \mathscr{D}/(\nu N^2)$ which is a measure of the scales available to turbulence. More precisely, Re_b is the ratio of the scale of the largest eddies which are allowed to overturn before becoming suppressed by stratification (the Ozmidov scale) to the scale at which overturning is precluded by viscous forces (the Kolmogorov scale). Various studies have suggested that for stratified turbulence to be maintained, Re_b has to be larger than a critical value which is approximately 20 (Gregg 1987; Stillinger, Helland & Van Atta 1983; Smyth & Moum 2000). Various observational studies have measured the buoyancy Reynolds number and have shown that it is $O(10^2–10^3)$ in the oceanic thermocline or in energetic estuaries and inlets (Gargett, Osborn & Nasmyth 1984; Moum 1996; Geyer *et al.* 2010). In table 2, we present the Re_b values corresponding to cases considered in this section. Each value has been calculated at a short time after the saturation of the turbulent perturbation field. For all cases, Re_b remains of the same order as the value presented in the table for a considerable length of time (of the total lifecycle of the KH billow) before diminishing as turbulence decays. As the numbers in the table suggest, Re_b spans nearly a decade in our simulations and lies well within the range suggested by the oceanographic observations. Interestingly, the new relatively high-Re_b regime considered in this study (as compared with earlier DNS studies), coincides with the range in which a large number of secondary instabilities (absent in low-Re flows) emerge in the flow and prevent a direct upscale cascade through vortex merging.

5. Influence of stratification

It is well-known that background stratification can have a significant influence on the evolution of a mixing layer. Specifically, strong stratification can suppress vertical buoyancy flux by inhibiting vertical motions. This influence has been incorporated in various parametrization schemes for shear-induced mixing. Theoretical studies have also shown that the growth rate of primary shear instability (KH or other types) is primarily a function of Ri_0 (Corcos & Sherman 1976; Mashayek & Peltier 2012b). Large stratification slows the growth of the primary wave. The vertical extent of the primary instability at its maximum amplitude is inversely related to the stratification and so is the extent of vertical entrainment of the layer after turbulent collapse. It was shown in Mashayek & Peltier (2012b) that stratification has a significant influence on the type and growth rate of secondary instabilities which grow on a primary wave. In particular, large stratification greatly suppresses vortex mergers due to inhibition of vertical motion, and it promotes the SCI of the cores (due to increase in the effective Rayleigh number across the unstable regions); it also promotes the SSI of the braid (by reducing the braid effective gradient Richardson number and also by diminishing the negative influence of the strain field on SSI), and it demotes the SPI (by diminishing the strength of the strain field from which the instability extracts its energy).

In the previous sections of this paper we showed that the Reynolds number may also influence the relative importance of these various modes of secondary instability (it promotes SCI and SSI, while SPI exists over an intermediate range of Re). Therefore, the path of the mixing layer from a laminar state to turbulence can be very different from one point to another in the Re–Ri_0 parameter space. To illustrate the combined influence of Re and Ri_0, we compare cases with low stratification ($Ri_0 = 0.04$) and high stratification ($Ri_0 = 0.12$, a high value in the context of KH instability) for various Reynolds numbers in figure 18. There are two primary differences between the low Ri_0 and high Ri_0 cases: first, vortex pairing in the form of two vortices orbiting each other before merging into one is observed for low Ri_0 whereas it is suppressed by high stratification in the $Ri_0 = 0.12$ cases; second, 3D perturbations in low-Ri_0 cases are primarily due to SCI, whereas at higher Ri_0, a number of stratification-induced secondary instabilities grow on the braid (such as SSI and SPI vortices) and/or in the cores (such as SVBI and LCVI). Therefore, the spanwise wavenumber spectrum of the high-Ri_0 cases is broader during the transition phase, which might have implications for the isotropy of turbulence and the efficiency of the related mixing.

Comparing cases with different Re at $Ri_0 = 0.04$, we observe an earlier emergence of 3D perturbations on the background KH wave with increase in Re. For $Re = 750$, at the onset of growth of $\mathcal{K}_{3D}$, pairing is well underway whereas for $Re = 10\,000$, the $\mathcal{K}_{3D}$ field is almost saturated by the time vortex cores begin to pair. This leads to early corrosion of vortex cores and suppression of the vertical motion associated with the pairing instability. This is consistent with the analyses presented in the previous section by means of spectral decomposition of the flow in the streamwise direction. It seems very likely that at even higher Re, 3D modes such as SSI and SCI may grow so early in flow evolution so as to completely prohibit the pairing instability through early and rapid destruction of the KH billow, similar to what is shown in the right column of the figure for $Ri_0 = 0.12$ cases (and which was discussed in detail in the last section). Our results suggest that for $Ri_0 = 0.04$, a higher Re than $10\,000$ is required to suppress the pairing mode to the extent that was observed in figure 13(b) by $Re = 8000$. However, such high Reynolds numbers are guaranteed to occur in geophysical environments. Therefore, in free shear layers in stratified oceans (although perhaps not in gravity currents), it is unlikely that pairing instability could play a
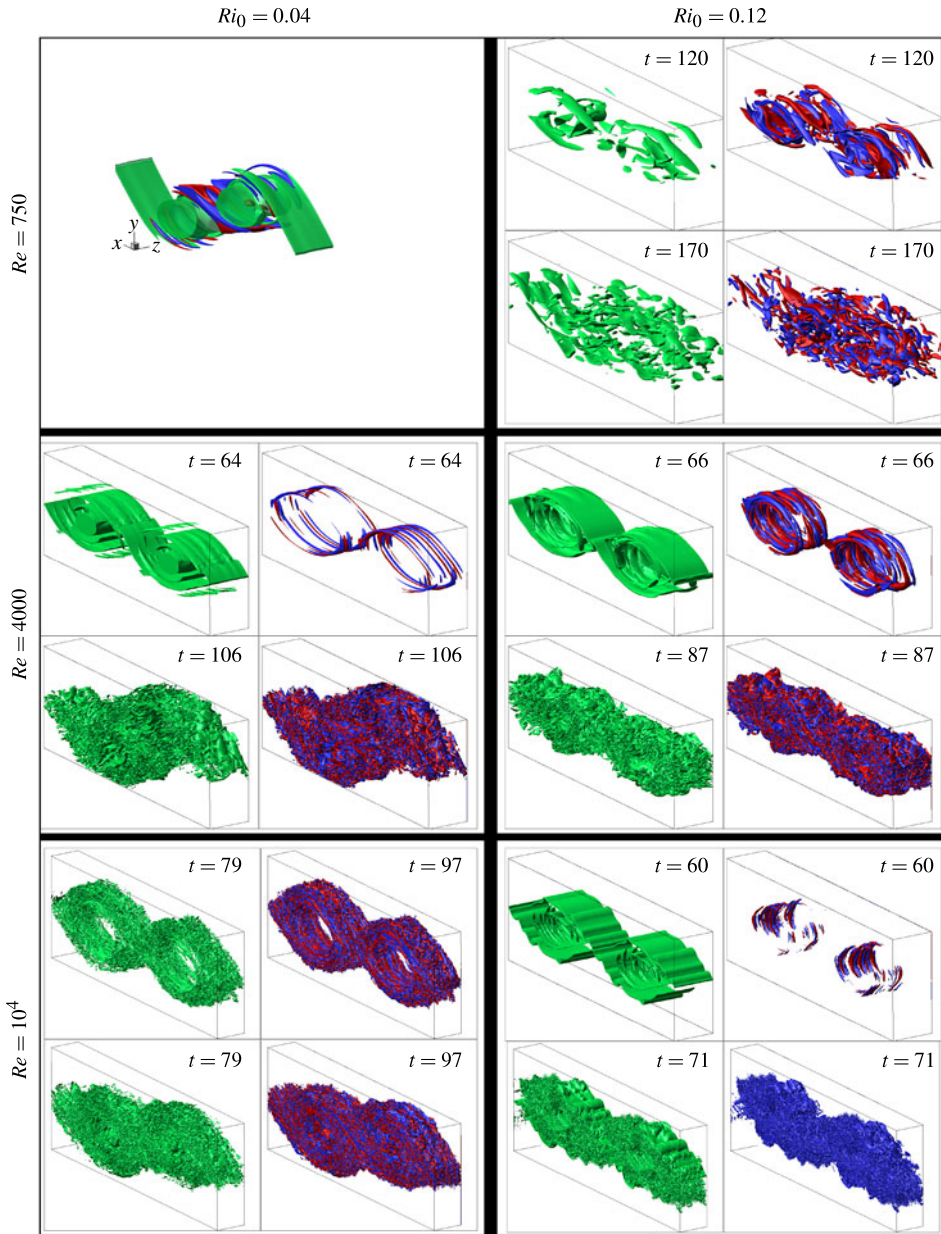
FIGURE 18. Influence of stratification at various Reynolds number on the evolution of the mixing layer.

dominant role in the transition process unless the flow were essentially unstratified (so that the 'zoo of secondary instabilities' specific to stratified flows would not exist), or there are perturbations (e.g. waves) in the environment which specifically favour vortex mergers. For the case of overflows and gravity currents, interactions between primary shear waves and the bottom boundary can facilitate relative streamwise motion between vortex cores which would help initiation of 'leapfrogging' motion of vortices
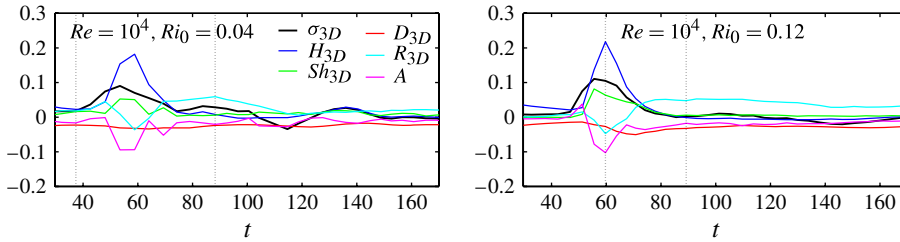
FIGURE 19. Comparison of energetics of evolution of 3D perturbations for low- and high-stratification cases both at $Re = 10\,000$.

which can lead to them merging. This depends upon specific characteristics of the overflow (such as its depth). Therefore, our conclusions regarding the suppression of vortex merging with increase in Ri_0 should not be extended to such flows.

To provide some quantitative information on the influence of the stratification on the energetics of the 3D perturbation field, figure 19 compares two cases, both with $Re = 10\,000$ but with different values of Ri_0. The main message of this figure is that 3D perturbations begin to grow earlier than the saturation time of the KH billow (t_{2D}) once Ri_0 is sufficiently large. This is due to promotion of both SCI in the vortex cores and SSI on the braid with increase in Ri_0. Therefore, as mentioned earlier with regards to interpretation of the observations of Geyer *et al.* (2010), it may well be that high values of Ri_0 and Re in the flows they examined had excited very early growth of 3D secondary instabilities leading to rapid homogenization of density and vorticity inside the vortex cores, leaving braid regions as dominant components of the back scatter signal. This is a conjecture that should be subject to further investigation. Another important point can be made based on figure 19: due to the action of vortex pairing at $Ri_0 = 0.04$, namely that the flow stabilizes eventually into a 'balanced' turbulent state (in which the balance is between $\mathcal{R}_{3D}$ and $\mathcal{D}_{3D}$), and therefore the commonly used correlations which relate dissipation to vertical diffusivity (by assuming a steady isotropic flow and a $\mathcal{R}_{3D}$–$\mathcal{D}_{3D}$ balance) becomes relevant over an even shorter time window of the lifecycle of the mixing layer (as compared with that which characterizes the $Ri_0 = 0.12$ case).

Finally, as a further demonstration of the significance of route to turbulence for mixing, we compare the influence of pairing on mixing efficiency and the effective vertical flux for two cases with $Ri_0 = 0.04$ and $Ri_0 = 0.12$ both for $Re = 4000$ in figure 20. Figure 20(*a*) compares the PSDs for the pairing mode as well as the primary KH wave (thin lines) between the two cases. Clearly, at low stratification the pairing mode dominates the power spectrum. This is associated with the pairing in the classical form, which involves orbiting of vortices prior to merging and which involves significant vertical motion and entrainment. For the intermediate stratification case ($Ri_0 = 0.12$), however, the upscale component of the energy cascade involves much less vertical motion. Nevertheless, it was shown in the last section that the upscale turbulent cascade (which is increasingly strongly suppressed with increase in Re) has important implications for mixing properties. Figure 20(*b*) shows that low-Ri_0 pairing leads to higher mixing efficiency due to increased diapycnal mixing (due to significantly increased stirring of the flow because of the orbiting and merging motion of the vortices) at a lower-energy dissipation rate (due to lack of activity of stratification-specific secondary modes which exists at higher Ri_0, and also due
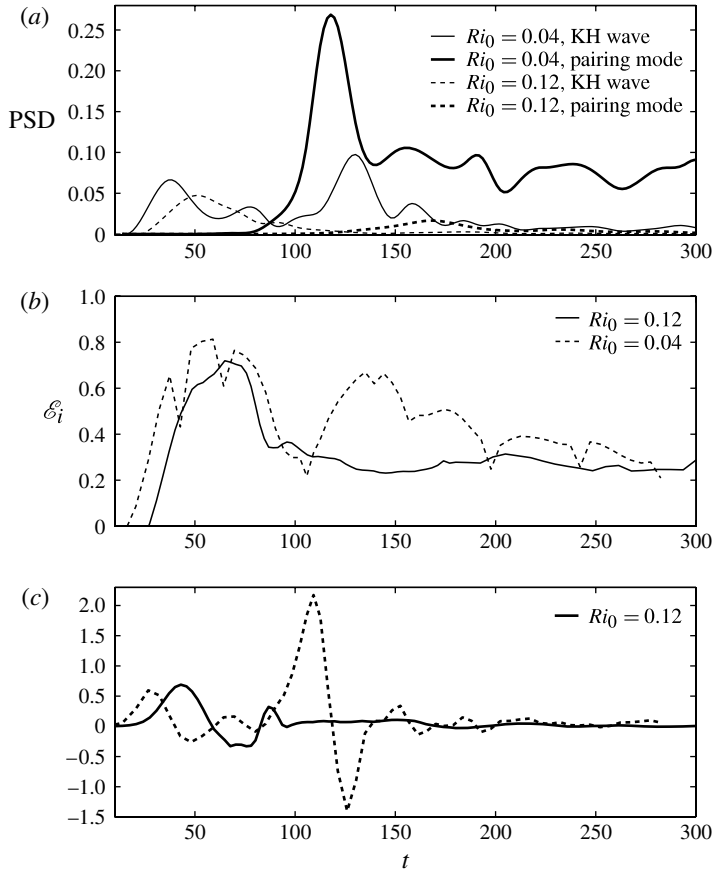
FIGURE 20. Investigating influence of stratification through Comparison of two cases with $Ri_0 = 0.04$ and $Ri_0 = 0.12$ both for $Re = 4000$: PSD in (*a*), instantaneous mixing efficiency in (*b*) and total buoyancy flux in (*c*).

to slight suppression of $\mathscr{K}_{3D}$ because of vortex pairing). Figure 20(*c*) illustrates the significant impact of vortex pairing on the buoyancy flux for the low stratification case. Therefore, consistent with the well-known inverse influence of stratification on vertical flux, mixing at low stratification can be more efficient and the effective flux can be larger. Therefore, the nature of shear-induced mixing at pycnocline depths in the ocean interior (with high stratification) can be very different from that which occurs in less strongly stratified regions of the deep ocean. Table 3 compares the effective diffusivity and efficiency of mixing values for the two cases discussed in figure 19 as well as for two cases at a lower Reynolds number.

6. A note on the combined influence of Pr, Re and Ri_0

Although Pr was fixed to one throughout this work, we are nevertheless in a position to offer some comment on the combined influence of Pr, Re and Ri_0 on the nature of the turbulence transition based on work of Mashayek & Peltier (2012*a*, 2011*b*). It was shown in Mashayek & Peltier (2012*a*) (by means of predictions based upon the use of an heuristic model) that increase in Pr has a suppressing

Re	Ri_0	$\langle \rho w \rangle /(\mathrm{d}\bar{\rho}/\mathrm{d}z)$	κ_{Osborn}, $\mathscr{E} = 0.15$	κ_{Osborn}, $\mathscr{E} = \mathscr{E}(t)$	$\mathscr{E}_c$	$\mathscr{E}_c$, post-t_{3D}
750	0.04	7.4×10^{-4}	1.7×10^{-4}	2.5×10^{-4}	0.35	0.3
750	0.12	5.1×10^{-4}	1.9×10^{-4}	2.2×10^{-4}	0.3	0.2
4000	0.04	14.9×10^{-4}	2.9×10^{-4}	6.5×10^{-4}	0.5	0.5
4000	0.12	6.19×10^{-4}	2.3×10^{-4}	3.3×10^{-4}	0.36	0.29

TABLE 3. Influence of stratification on mixing efficiency and effective diffusivity. All parameters were defined in § 4 (see figure 16 and the related discussions).

influence on the SSI (by increasing the effective gradient Richardson number of the braid), a promoting influence on SPI (by increasing the strength of the strain field from which SPI extracts its energy) and a slight promoting influence on SCI (by slowing down the decay of the density difference across the core unstable regions). Therefore, within the ranges of Pr associated with atmospheric flows or thermally stratified oceanic flows (such as those of van Haren & Gostiaux (2010, 2012)), the following changes are expected to be characteristic of any of the cases considered in this study: at a constant Re and Ri_0, increase in Pr will lead to reduced SSI activity on the braid, a stronger SPI vortex at the stagnation point and a dominant role played by SCI in the transition process. As shown by Mashayek & Peltier (2011*b*), increase in Pr also promotes the intensity of core activity such as SSI of the vorticity layers inside the cores, and Rayleigh–Taylor instability. This, along with the suppression of the SSI on the braid with increase in Pr implies the increased importance of the homogenization of the core region relative to that of the braid with increase in Pr. This gives further support to our conjecture that the lack of existence of core structure in the observations of KH waves by Geyer *et al.* (2010) is due to early homogenization of cores since their observations were made in salt stratified estuaries with very high Prandtl numbers.

7. Discussion and conclusions

We have herein studied the influence of Re and Ri_0 on the mechanisms responsible for the turbulence transition and related mixing in free shear layers using high-resolution numerical simulations. The range of Re values considered was high compared with those which have previously been employed in the existing body of numerical studies and this has enabled us to establish a much closer connection to geophysical shear layers.

The theoretical predictions of Mashayek & Peltier (2012*a*,*b*) regarding the type and characteristics of secondary instabilities which are expected to grow on a KH billow were verified using these quantitative analyses. It was shown that most mechanisms responsible for turbulent collapse of the shear layer at sufficiently high Re are highly three-dimensional. Therefore, any implications of the results of 2D numerical experiments (which are prevalent in the literature) for mixing in shear flows should be regarded with scepticism. Specifically, it has been shown that three-dimensional instabilities such as the SCI of the core (Klaassen & Peltier 1985*b*) and SPI of the braid (Mashayek & Peltier 2012*a*) both play a critical role in turbulence collapse of the mixing layer with the former playing the dominant role. Even though secondary shear induced vortices on the braid were shown to proliferate, to grow more rapidly and to arise earlier in flow evolution with increase in Re, the SCI remains the

dominant mode in mediating transition within the Re–Ri_0 parameter range explored in this study. It was also shown that braid instabilities such as the SSI may also excite the onset of several additional instabilities (such as SCI, or Rayleigh–Taylor instability) inside the cores. In fact, it was predicted in Mashayek & Peltier (2012*a*) and verified in this work that the vorticity layers inside the core can become shear unstable themselves, provided that Re is sufficiently high (at a given Ri_0 and Pr). It is conceivable that for extremely high Reynolds numbers, the initial vorticity layer from which the KH billow evolves might become secondary shear unstable very early in flow evolution, leading to rapid homogenization of the cores. Alternatively, it might well be that the cores become homogenized prior to the development of the braid through a series of secondary instabilities as was shown for the $Re > 4000$ cases of this study. Both possibilities might be contributing to the absence of core structures in the oceanic observations of KH waves reported in Geyer *et al.* (2010).

Our study has been focused upon the characteristic change in the nature of the transition to turbulence that occurs from low Reynolds numbers (associated with laboratory experiments and the existing body of numerical studies) to high Reynolds numbers (associated with geophysical flows). Laboratory and numerical experiments have established that at relatively low Reynolds numbers, a number of large-scale instabilities (such as 2D or 3D vortex interactions such as pairing or formation of vortex tubes) play key roles in the turbulent collapse of the shear layer, and that secondary core instability is the dominant mode responsible for introducing small-scale 3D perturbations into the flow field. At high Re, however, a large number of secondary instabilities, the number of which increases with Re, emerge on the background primary KH instability. The growth rate of these instabilities increases and their time of formation becomes earlier with increase in Re. It was shown that at sufficiently high Re, primary vortex cores break down to turbulence very rapidly upon formation through emergence of a number of small-scale secondary instabilities and the inverse cascade through vortex-merging instabilities is also thereby suppressed. This is summarized in figure 21 which illustrates a two-stage suppression of the inverse cascade with increase in Re. Although the suppressing influence of stratification on vortex pairing has long been known, the analyses reported here are believed to be the first to demonstrate that the turbulent collapse of the billow itself has a similarly inhibiting influence on the upscale cascade of energy as the Reynolds number increases. This has implications for the relevance of the body of literature on vortex-merging instabilities for geophysical flows. This view also appears to be consistent with lack of observations of vortex mergers in observed KH wave trains in geophysical environments (Geyer *et al.* 2010; van Haren & Gostiaux 2010; Luce *et al.* 2010; Fukao *et al.* 2011).

We have demonstrated herein that the 'route to turbulence' matters insofar as several important characteristics of shear turbulence (such as the efficiency of diapycnal mixing and the related effective diffusivity) are concerned. It was shown that the number of secondary instabilities which grow on a background primary shear instability, and their order of appearance have significant implications for flow characteristics such as the onset of transition, the extent to which the flow is isotropic and the extent to which the turbulent phase is stationary. These analyses have established that the breakdown of certain assumptions built into commonly employed correlations used to infer eddy diffusivities can lead to significant errors. More specifically, we examined relation (1.1) as an example of a commonly employed relationship and showed that its predictions for effective diffusivity are in acceptable agreement with those calculated accurately from numerical simulation only in the
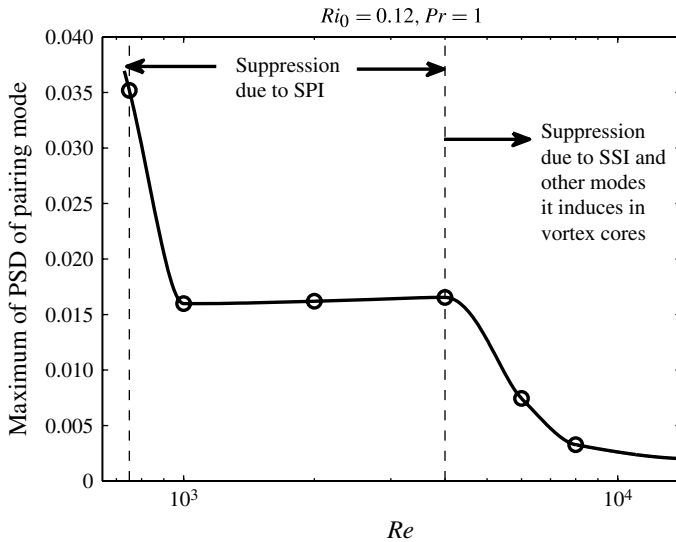
FIGURE 21. Maximum PSD for the pairing instability for various Reynolds numbers all at $Ri_0 = 0.12$. The circles correspond to the peaks of the curves in figure 13(b).

fully developed turbulent phase. However, insofar as the vertical flux of buoyancy is concerned, such relations introduce large errors by ignoring the early stages of flow evolution in which the flow is more coherently structured and less isotropic and stationarily turbulent. This was shown to be the largest source of error according to our analyses. Another source of error often associated with observational-based estimates made through the use of relation (1.1) is in measurements of the rate of energy dissipation which has not been fully discussed in the present paper. Our estimates of effective diffusivity are in the range of those associated with the abyssal ocean implying a consistency with the increasingly stronger assumption that shear instability is one of the primary mechanisms responsible for deep ocean mixing at the subgrid scale in OGCMs.

Even though our analyses show that the efficiency of mixing can differ significantly (by more than 200 %) over the range of parameters considered herein, it seems that the dissipation rate partially adjusts itself in such a way that the affect of variations in efficiency is not as significant on the calculated diffusivities. Therefore, our analyses show that a mean value of $\mathscr{E} \sim 1/3$ along with relation (1.1) should provide acceptably high-quality predictions of time-averaged effective diffusivity for sufficiently high Reynolds numbers, provided that the proper time history of dissipation rate is employed in the relation. Since this is not feasible in the context of large-scale oceanographic modelling, estimates of shear-based effective diffusion of buoyancy made from observations will suffer not only for the reasons explained above, but also from the lack of correlation between the rate of energy dissipation and the efficiency of mixing in the available parametrization schemes. Moreover, it is important to note that the assumption of isotropy behind the Osborn formula needs to be analysed in more detail since our analyses revealed a non-significant contribution of anisotropy to the energy balance of the perturbation field in the turbulent phase of the flow. The value of 1/3 suggested herein agrees surprisingly well with the predictions of Caulfield, Tang & Plasting (2004) for an upper bound on the efficiency at high
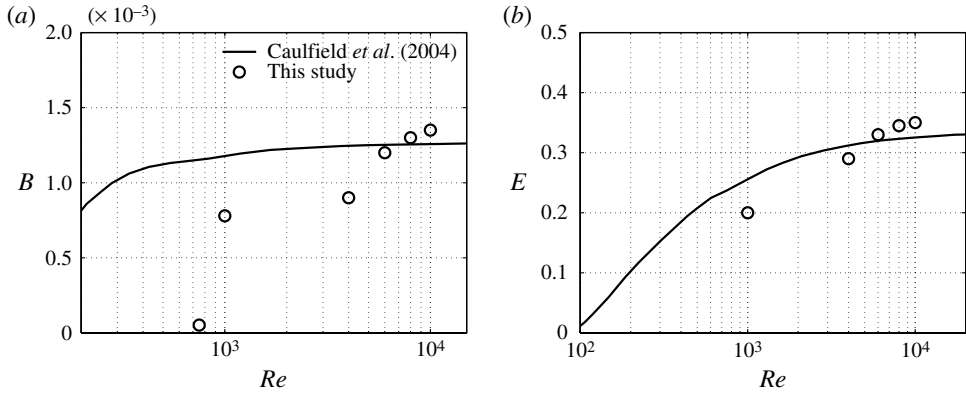
FIGURE 22. Comparison of the time-averaged (over the turbulent phase of the flows) buoyancy flux (*a*) and mixing efficiency (*b*) values obtained from the numerical experiments discussed in this work and theoretical predictions of Caulfield *et al.* (2004) for upper bounds on the two parameters as a function of the Reynolds number.

Reynolds numbers. This is shown in figure 22(*b*). Also shown in the figure is a comparison between the corresponding turbulent buoyancy fluxes. The study of Caulfield *et al.* (2004) considered plane Couette flows as a basis for calculation of the upper bound, and the methodology used therein makes it hard to assess the role of walls on the mixing process. If it could be shown that the role of the walls was negligible, then figure 22 can be taken to suggest that high-*Re* KH billows discussed herein mix as efficiently as possible. It will be of interest to investigate whether this is a characteristic of KH waves in particular, or whether other primary shear instabilities may mix as efficiently. Moreover, it will be important to study not just one, but multiple lifecycles of instability of shear layers to obtain a mixing efficiency averaged over a sufficiently long period to enable a direct comparison to estimates of efficiency and diffusivity based on observations. Therefore, until further studies are performed, this study together with that of Caulfield *et al.* (2004) provides strong evidence that the often employed universal value of 0.2 for $\mathscr{E}$ needs to be revised.

Finally, we will summarize the work reported herein with five concluding remarks. First, the route to turbulence can be an important factor in the determination of turbulence properties. Although this might not be encouraging insofar as turbulence parametrization is concerned, it cannot be ignored. Second, the assumption that turbulence efficiency may be well-approximated by the value $\mathscr{E} = 0.2$ is suspect based upon the evidence provided herein. Furthermore, there is no reason to believe that the globally averaged value for $\mathscr{E}$ may be approximated as 0.2 either and this can be an important source of error in estimates of ocean energy budgets. Proper parametrization of the efficiency of mixing based on background flow parameters such as the stratification level, shear and strain will improve estimates of mixing properties greatly both at small scale and on the global scale. Third, this work along with that reported in Mashayek & Peltier (2012*a*,*b*) demonstrates that there is a characteristic change in the properties of shear-induced turbulence as the Reynolds numbers increases from the low values characteristic of laboratory experiments to the much higher Reynolds numbers associated with geophysical flows. This is due primarily to the suppression of the inverse cascade of energy with increase in
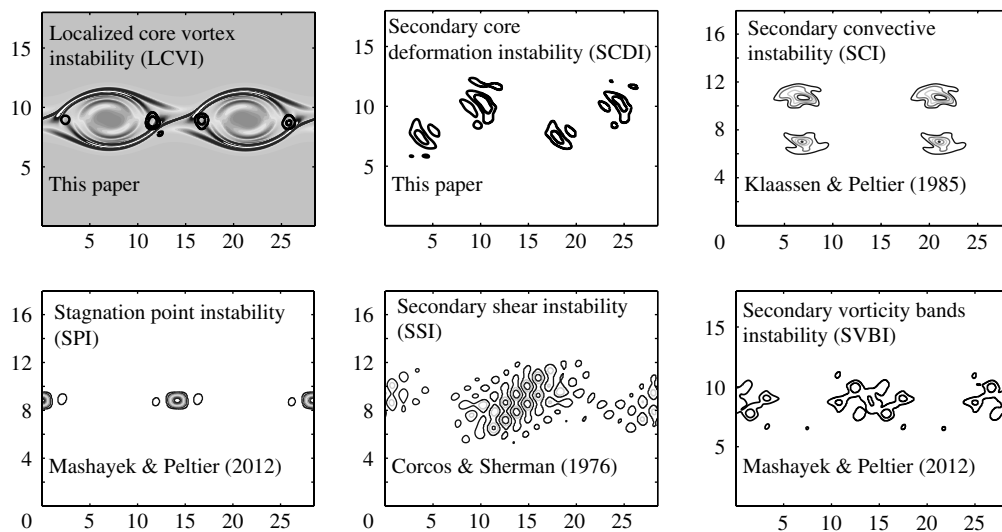
FIGURE 23. Lexicon of various secondary instabilities discussed in Mashayek & Peltier (2012*a*,*b*). Each frame contains the reference to the original study which provides details of its corresponding instability. The horizontal and vertical axes correspond to *x* and *z* coordinates, respectively. The underlying background KH wave is shown in the first panel to provide the reference of the KH wave basic state in terms of which the location of each instability is illustrated in other frames of the figure.

Reynolds number because of the emergence of small-scale structures which only exist at sufficiently high Reynolds numbers. Fourth, this work along with Mashayek & Peltier (2012*a*,*b*, 2011*b*) demonstrates that the combined influence of Reynolds, Richardson and Prandtl number on stratified shear turbulence is complex due to the influence of each of these parameters on the route to turbulence through their influence upon the types and number of secondary and higher-order instabilities which grow on the primary shear instability. Thus, any parametrization of shear mixing should be inclusive of all the primitive parameters involved in the definitions of *Re*, *Pr* and *Ri*$_0$. Finally, it is also important to note that the remarks made in this concluding paragraph are not specific to a particular shear instability. Numerous shear-induced processes which lead to diapycnal mixing in the ocean are periodic or episodic in nature and involve various stages of flow evolution with the coherence of flow structures, level of turbulence and properties of turbulence varying significantly between the various stages.
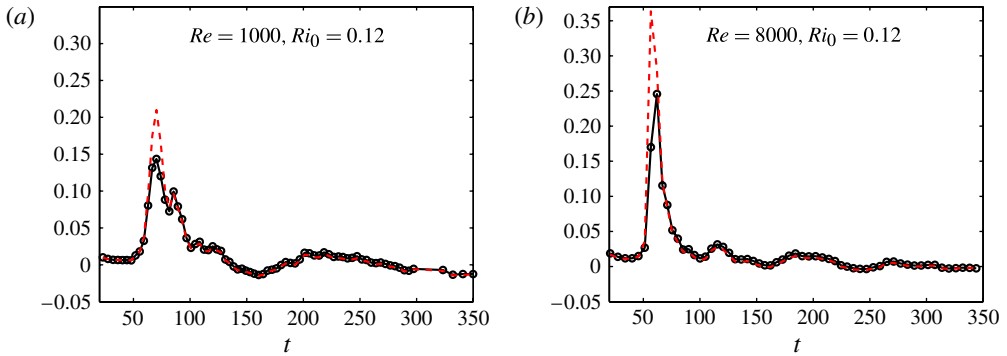
Acknowledgements

FIGURE 24. (Colour online) Comparison of the left-hand side (dashed) and right-hand side (solid black with circles) of (2.18) for two cases of table 1.

Appendix A. Secondary instability names

There are frequent references to various secondary instabilities in this article by using their corresponding acronyms. Figure 23 provides a secondary instability lexicon to help reminding the reader of what instability each acronym refers to.

Appendix B. Verification of the accuracy of numerical simulations

Figure 24 shows a comparison of the left-hand side and right-hand side of (2.18) for two cases of table 1. Note that the two sides of (2.18) are independently calculated from simulation results. The slight differences at the peaks of the curves is due to the fact that left-hand side of equation is calculated using central difference differentiation of the instantaneous kinetic energy of the calculation. Thus, the accuracy of the plotted left-hand side depends heavily on the frequency of saving of output files during the simulation. This frequency is limited by computational resources. During time intervals of large gradients (such as the peaks in figure 24), fewer data points would result in error in calculation of σ_{3D} (and not of the simulation itself). More frequent saving of output files would improve the agreement between the curves at their peaks. Figure 24 clearly shows that the flows are resolved throughout flow evolution and particularly during the turbulent phase (i.e. beyond the curve peaks).

REFERENCES

AUCAN, J., MERRIFIELD, M. A., LUTHER, D. S. & FLAMENT, P. 2006 Tidal mixing events on the deep flanks of Kaena Ridge, Hawaii. *J. Phys. Oceanogr.* **36**, 1202–1219.

BALMFORTH, N. J., ROY, A. & CAULFIELD, C. P. 2012 Dynamics of vorticity defects in stratified shear flow. *J. Fluid Mech.* **694**, 292–331.

CARPENTER, J. R., BALMFORTH, N. J. & LAWRENCE, G. A. 2010a Identifying unstable modes in stratified shear layers. *Phys. Fluids* **22**, 1–13.

CARPENTER, J. R., LAWRENCE, G. A. & SMYTH, W. D. 2007 Evolution and mixing of asymmetric Holmboe instabilities. *J. Fluid Mech.* **582**, 103–132.

CARPENTER, J. R., TEDFORD, E. W., RAHMANI, M. & LAWRENCE, G. A. 2010b Holmboe wave fields in simulation and experiment. *J. Fluid Mech.* **648**, 205–223.

CAULFIELD, C. P. 1994 Multiple linear instability of a layered stratified shear flow. *J. Fluid Mech.* **258**, 155–285.

CAULFIELD, C. & PELTIER, W. R. 2000 Anatomy of the mixing transition in homogeneous and stratified free shear layers. *J. Fluid Mech.* **413**, 1–47.

CAULFIELD, C. P., TANG, W. & PLASTING, S. C. 2004 Reynolds number dependence of an upper bound for the long-time-averaged buoyancy flux in plane stratified couette flow. *J. Fluid Mech.* **498** (1), 315–332.

CAULFIELD, C. P., YOSHIDA, S. & PELTIER, W. R. 1996 Secondary instability and three-dimensionalization in a laboratory accelerating shear layer. *Dyn. Atmos. Oceans* **23**, 125–138.

CORCOS, G. & SHERMAN, F. 1976 Vorticity concentration and the dynamics of unstable free shear layers. *J. Fluid Mech.* **73**, 241–264.

CORTESI, A. B., YADIGAROGLU, G. & BANNERJEE, S. 1998 Numerical investigation of the formation of three-dimensional structures in stably stratified mixing layers. *Phys. Fluids* **10**, 1449–1473.

DRAZIN, P. G. & REID, W. H. 1981 *Hydrodynamic Stability*. Cambridge University Press.

FUKAO, S., LUCE, H., MEGAC, T. & YAMAMOTO, M. K. 2011 Extensive studies of large-amplitude Kelvin–Helmholtz billows in the lower atmosphere with VHF middle and upper atmosphere radar. *Q. J. R. Meteorol. Soc.* **137**, 1019–1041.

GARGETT, A. E., OSBORN, T. R. & NASMYTH, P. W. 1984 Local isotropy and the decay of turbulence in a stratified fluid. *J. Fluid Mech.* **144** (1), 231–280.

GEMMRICH, J. R. & VAN HAREN, H. 2001 Thermal fronts generated by internal waves propagating obliquely along the continental slope. *J. Phys. Oceanogr.* **31**, 649–655.

GEYER, W. R., LAVERY, A. C., SCULLY, M. E. & TROWBRIDGE, J. H. 2010 Mixing by shear instability at high Reynolds number. *Geophys. Res. Lett.* **37**, L22607.

GOSSARD, E. E. 1990 Radar research on the atmospheric boundary layer. In *Radar in Meteorology* (ed. D. Atlas). pp. 477–527. American Meteorological Society.

GREGG, M. C. 1987 Diapycnal mixing in the thermocline: a review. *J. Geophys. Res.* **92** (C5), 5249–5286.

GRIFFITHS, S. D. & PELTIER, W. R. 2009 Modelling of polar ocean tides at the last glacial maximum: amplification, sensitivity, and climatological implications. *J. Clim.* **22**, 2905–2924.

HELMHOLTZ, P. 1868 XLIII. On discontinuous movements of fluids. *Philos. Mag.* **36** (244), 337–346.

HOLMBOE, J. 1962 On the behaviour of symmetric waves in stratified shear layers. *Geofys. Publ. Oslo* **24**, 67–113.

HOWARD, 1961 Note on a paper of John W. Miles. *J. Fluid Mech.* **10**, 509–512.

JAYNE, S. R. & LAURENT, L. C. ST. 2001 Parameterizing tidal dissipation over rough topography. *Geophys. Res. Lett.* **28**, 811–814.

KELVIN, LORD 1871 Hydrokinetic solutions and observations. *Phil. Mag.* **10**, 155–168.

KLAASSEN, G. P. & PELTIER, W. R. 1985a The effect of Prandtl number on the evolution and stability of Kelvin–Helmholtz billows. *Geophys. Astrophys. Fluid Dyn.* **32**, 23–60.

KLAASSEN, G. P. & PELTIER, W. R. 1985b The onset of turbulence in finite amplitude Kelvin–Helmholtz billows. *J. Fluid Mech.* **155**, 1–35.

KLAASSEN, G. P. & PELTIER, W. R. 1989 The role of transverse secondary instabilities in the evolution of free shear layers. *J. Fluid Mech.* **202**, 367–402.

LAURENT, L. ST. & SIMMONS, H. 2006 Estimates of power consumed by mixing in the ocean interior. *J. Clim.* **19**, 4877–4890.

LAURENT, L. C. ST., SIMMONS, H. L. & JAYNE, S. R. 2002 Estimates of tidally driven enhanced mixing in the deep ocean. *Geophys. Res. Lett.* **29** (23), 2106.

LEDWELL, J. R., MONTGOMERY, E. T., POLZIN, K. L., LAURENT, L. C. ST., SCHMITT, R. W. & TOOLE, J. M. 2000 Evidence for enhanced mixing over rough topography in the abyssal ocean. *Nature* **403**, 182–189.

LEDWELL, J. R., WATSON, A. J. & LAW, C. S. 1993 Evidence for slow mixing across the pycnocline from an open ocean tracer release experiment. *Nature* **364**, 701–703.

LEDWELL, J. R., WATSON, A. J. & LAW, C. S. 1998 Mixing of a tracer in the pycnocline. *J. Geophys. Res.* **103**, 21499–21529.

LEE, V. & CAULFIELD, C. P. 2001 Nonlinear evolution of a layered stratified shear flow. *Dyn. Atmos. Oceans* **34**, 103–124.

LEGG, S. 2009 Improving oceanic overflow representation in climate models: the gravity current entrainment climate process team. *Bull. Am. Meteorol. Soc.* **90**, 657–670.

LEY, B. E. & PELTIER, W. R. 1978 Wave generation and frontal collapse. *J. Atmos. Sci.* **35**, 3–17.

LUCE, H., MEGA, T., YAMAMOTO, M. K., YAMAMOTO, M., HASHIGUCHI, H., FUKAO, S., NISHI, N., TAJIRI, T. & NAKAZATO, M. 2010 Observations of Kelvin–Helmholtz instability at a cloud base with the middle and upper atmosphere (MU) and weather radars. *J. Geophys. Res.* **115**, D19116.

MARSHALL, J. & SPEER, K. 2012 Closure of the meridional overturning circulation through southern ocean upwelling. *Nature Geosci.* **5**, 171–180.

MASHAYEK, A. & PELTIER, W. R. 2011*a* Three-dimensionalization of the stratified mixing layer at high Reynolds number. *Phys. Fluids* **23**, 111701.

MASHAYEK, A. & PELTIER, W. R. 2011*b* Turbulence transition in stratified atmospheric and oceanic shear flows: Reynolds and Prandtl number controls upon the mechanism. *Geophys. Res. Lett.* **38**, L16612.

MASHAYEK, A. & PELTIER, W. R. 2012*a* The 'zoo' of secondary instabilities precursory to stratified shear flow transition. Part 1. Shear aligned convection, pairing, and braid instabilities. *J. Fluid Mech.* **708**, 5–44.

MASHAYEK, A. & PELTIER, W. R. 2012*b* The 'zoo' of secondary instabilities precursory to stratified shear flow transition. Part 2. The influence of stratification. *J. Fluid Mech.* **708**, 45–70.

MILES, J. W. 1961 On the stability of heterogeneous shear flows. *J. Fluid Mech.* **10**, 496–508.

MOUM, J. N. 1996 Energy-containing scales of turbulence in the ocean thermocline. *J. Geophys. Res.* **101**, 14095–14109.

MOUM, J. N., FARMER, D. M., SMITH, W. D., ARMI, L. & VAGLE, S. 2003 Structure and generation of turbulence at interfaces strained by internal solitary waves propagating shoreward over the continental shelf. *J. Phys. Oceanogr.* **33**, 2093–2112.

MUNK, W. H. 1966 Abyssal recipes. *Deep-Sea Res.* **113**, 207–230.

MUNK, W. H. & WUNSCH, C. 1998 Abyssal recipes II: energetics of tidal and wind mixing. *Deep-Sea Res.* **45**, 1977–2010.

NIKURASHIN, M. & LEGG, S. 2011 A mechanism for local dissipation of internal tides generated at rough topography. *J. Phys. Oceanogr.* **41**, 378–395.

OSBORN, T. R. 1980 Estimates of the local rate of vertical diffusion from dissipation measurements. *J. Phys. Oceanogr.* **10**, 83–89.

PELTIER, W. R. & CAULFIELD, C. 2003 Mixing efficiency in stratified shear flows. *Annu. Rev. Fluid Mech.* **35**, 135–167.

PELTIER, W. R. & CLARK, T. L. 1979 The evolution and stability of finite amplitude mountain waves. Part II: surface wave drag and severe downslope windstorms. *J. Atmos. Sci.* **36**, 1498–1529.

PELTIER, W. R. & SCINOCCA, J. F. 1990 The origin of severe downslope windstorm pulsations. *J. Atmos. Sci.* **47**, 2853–2870.

PHAM, H. T., BRUCKER, S. & SARKARAND, K. 2009 Dynamics of a stratified shear layer above a region of uniform stratification. *J. Fluid Mech.* **630**, 191–223.

PHAM, H. T. & SARKAR, S. 2010 Transport and mixing of density in a continuously stratified shear layer. *J. Turbul.* **24**, 1–23.

POLZIN, K. L., TOOLE, J. M., LEDWELL, J. R. & SCHMITT, R. W. 1997 Spatial variability of turbulent mixing in the abyssal ocean. *Science* **276**, 93–96.

SALEHIPOUR, H., STUHNE, G. R. & PELTIER, W. R. 2013 A higher order discontinuous Galerkin, global shallow water model: global ocean tides and aquaplanet benchmarks, *Ocean Model.* (submitted).

SMYTH, W. D. 2003 Secondary Kelvin–Helmholtz instability in weakly stratified shear flow. *J. Fluid Mech.* **497**, 67–98.

SMYTH, W. D., CARPENTER, J. R. & LAWRENCE, G. A. 2007 Mixing in symmetric holmboe waves. *J. Phys. Oceanogr.* **37**, 1566–1583.

SMYTH, W. D., KLAASSEN, G. P. & PELTIER, W. R. 1988 Finite amplitude Holmboe waves. *Geophys. Astrophys. Fluid Dyn.* **43** (2), 181–222.

SMYTH, W. D. & MOUM, J. N. 2000 Length scales of turbulence in stably stratified mixing layers. *Phys. Fluids* **12**, 1327.

SMYTH, W. D., MOUM, J. & CALDWELL, D. 2001 The efficiency of mixing in turbulent patches: inferences from direct simulations and microstructure observations. *J. Phys. Oceanogr.* **31**, 1969–1992.

SMYTH, W. D. & PELTIER, W. R. 1991 Instability and transition in finite amplitude Kelvin–Helmholtz and Holmboe waves. *J. Fluid Mech.* **228**, 387–415.

SMYTH, W. D. & PELTIER, W. R. 1994 Three-dimensionalization of barotropic vortices on the f-plane. *J. Fluid Mech.* **265**, 25–64.

SMYTH, W. D. & WINTERS, K. B. 2003 Turbulence and mixing in Holmboe waves. *J. Phys. Oceanogr.* **33**, 694–711.

STAQUET, 2000 Mixing in a stably stratified shear layer: two- and three-dimensional numerical experiments. *Fluid. Dyn. Res.* **27**, 367–404.

STILLINGER, D. C., HELLAND, K. N. & VAN ATTA, C. W. 1983 Experiments on the transition of homogeneous turbulence to internal waves in a stratified fluid. *J. Fluid Mech.* **131**, 91–122.

SUTHERLAND, B. R., CAULFIELD, C. P. & PELTIER, W. R. 1994 Internal gravity wave generation and hydrodynamic instability. *J. Atmos. Sci.* **51**, 3261–3280.

SUTHERLAND, B. R. & PELTIER, W. R. 1994 Turbulence transition and internal wave generation in density stratified jets. *Phys. Fluids* A **6**, 1267–1284.

TAYLOR, G. I. 1931 Effect of variation in density on the stability of superposed streams of fluid. *Proc. R. Soc. Lond.* A **132**, 499–523.

THORPE, S. A. 2005 *The Turbulent Ocean*. Cambridge University Press.

VAN HAREN, H. & GOSTIAUX, L. 2010 A deep-ocean Kelvin–Helmholtz billow train. *Geophys. Res. Lett.* **37**, L03605.

VAN HAREN, H. & GOSTIAUX, L. 2012 Detailed internal wave mixing above a deep-ocean slope. *J. Mar. Res.* **70**, 173–197.

WINTERS, K., LOMBARD, P., RILEY, J. & D'ASARO, E. A. 1995 Available potential energy and mixing in density-stratified fluids. *J. Fluid Mech.* **289**, 115–128.

WUNSCH, C. & FERRARI, R. 2004 Vertical mixing, energy, and the general circulation of the oceans. *Annu. Rev. Fluid Mech.* **36**, 28–314.